Earth Syst. Sci. Data, 17, 2463–2488, 2025
https://doi.org/10.5194/essd-17-2463-2025

Open Access Earth System Science Data

HHU24SWDSCS: a shallow-water depth model over island areas in the South China Sea retrieved from satellite-derived bathymetry

Yihao Wu[1,★], Hongkai Shi[2,★], Dongzhen Jia[2], Ole Baltazar Andersen[3], Xiufeng He[2], Zhicai Luo[4], Yu Li[2], Shiyuan Chen[2], Xiaohuan Si[2], Sisu Diao[2], Yihuang Shi[2], and Yanglin Chen[2]

[1]School of Geomatics Science and Technology, Nanjing Tech University, Nanjing, 211816, China
[2]School of Earth Sciences and Engineering, Hohai University, Nanjing, 211100, China
[3]DTU Space, Technical University of Denmark, Lyngby, 2800, Denmark
[4]MOE Key Laboratory of Fundamental Physical Quantities Measurement, School of Physics, Huazhong University of Science and Technology, Wuhan, 430074, China
★These authors contributed equally to this work.

Correspondence: Hongkai Shi (shk@hhu.edu.cn) and Dongzhen Jia (jdz@hhu.edu.cn)

Received: 28 September 2024 – Discussion started: 23 October 2024
Revised: 28 February 2025 – Accepted: 10 March 2025 – Published: 10 June 2025

Abstract. Accurate shallow-water depth information for island areas is crucial for maritime safety, resource exploration, ecological conservation, and offshore economic activity. Traditional approaches such as shipborne sounding and airborne bathymetric light detection and ranging (lidar) surveys are expensive, time-consuming, and constrained in politically sensitive regions. Moreover, satellite-altimetry-predicted depths exhibit large errors over shallow waters. In contrast, satellite-derived bathymetry (SDB), estimated from multispectral imagery, provides a rapid, open-source, and cost-effective technique for comprehensively characterizing the bathymetry of a region. Given the scarcity of in situ water depth data for the South China Sea (SCS), a shallow-water depth model, HHU24SWDSCS (Hohai University 2024 Shallow-Water Depth Model of South China Sea), was developed using a linear band model by integrating 1298 Ice, Cloud, and land Elevation Satellite-2 (ICESat-2) tracks with 70 Sentinel-2 multispectral images. The model covers over 120 islands and reefs in the SCS region at a resolution of 10 m. Validation against independent ICESat-2 depth data yielded a root mean square error for the model of 0.53–1.24 m (< 5 % of the maximum depth). Further validation using independent airborne lidar bathymetry data in the Lingyang Reef demonstrated an accuracy of 1.01 m. Comparisons with existing bathymetry models revealed the superior performance of the developed model. While traditional bathymetry models exhibit errors of up to tens of meters or larger over island regions and should therefore be used with caution, HHU24SWDSCS demonstrated good accuracy in shallow waters across the SCS. This model thus provides a reference for mapping shallow-water depth close to islands and provides fundamental support for research in oceanography, geodesy, and other disciplines. The HHU24SWDSCS data are freely available at https://doi.org/10.5281/zenodo.13852568 (Wu et al., 2024a).

Published by Copernicus Publications.

1 Introduction

Shallow-water bathymetry, which is critically important for maritime safety, ecological conservation, and marine economic development (Cesbron et al., 2021; Mavraeidopoulos et al., 2017; Wölfl et al., 2019; Yen et al., 2004), has long been a core research focus in oceanography, geophysics, and coastal geomorphology, profoundly influencing studies on ocean currents, Earth's gravity field, and seafloor sedimentation processes (Babonneau et al., 2013; Tinto et al., 2019; Wang et al., 2018b; Wu et al., 2024b). Moreover, since most marine-related human activities are concentrated in coastal shallow-water areas, accurate bathymetry information plays a pivotal role in port construction, marine fisheries, cross-sea bridge construction, and other marine economic and engineering activities (Bergstad et al., 2019; Parker, 2002; Šiljeg et al., 2019).

The South China Sea (SCS), one of the most active marine systems globally, is characterized by a complex bathymetry (Hwang, 1999; Pitcher et al., 2000; Su et al., 2018). In the central basin of the SCS, the bathymetry is deeper than 4000 m, yet it contains numerous islands, shoals, and banks, with depths < 100 m in the continental shelf region (Ruan et al., 2020). A thorough investigation of the shallow-water bathymetry in the SCS is crucial for conserving biodiversity, coral reef ecosystems, and marine fisheries; addressing coastal erosion; and exploring petroleum. Moreover, it is indispensable for achieving sustainable use of marine resources, promoting marine environmental protection, and fostering international cooperation (Folorunso and Li, 2015; Goodman et al., 2020; Misra and Ramakrishnan, 2020; Yen et al., 2004).

Traditional methods for obtaining bathymetry data primarily include shipborne sonar sounding, airborne bathymetric light detection and ranging (lidar), and satellite altimetry (An et al., 2024; Guenther, 2007; Smith and Sandwell, 1994). Shipborne sounding, and particularly multibeam sounding, is one of the most accurate methods, capable of emitting multiple pulses simultaneously in order to expand the survey range and achieve centimeter-level accuracy in water depth measurements (Costa et al., 2009; Ernstsen et al., 2006). However, shipborne surveys are limited in shallow and narrow waters, in which vessel-draft limitations, beam angles, and multipath effects significantly affect data quality and limit their availability (Costa et al., 2009; Hsu et al., 2021; Schneider von Deimling and Weinrebe, 2014). Airborne bathymetric lidar technology can rapidly obtain sub-meter-resolution bathymetric data. However, it is costly and its measurement accuracy is influenced by water quality, making it unsuitable for large-scale surveys (Tysiac, 2020). Over deep waters, satellite-altimetry-predicted depths play a dominant role in global bathymetry detection (Ge et al., 2025); however, this method faces challenges in coastal zones, and the predicted water depths exhibited high uncertainties in shallow waters (Ferreira et al., 2022). Furthermore, satellite-altimetry-predicted depths lack short-wavelength information (i.e., for wavelengths shorter than several kilometers) owing to the limited resolution of altimetry data, thus preventing their use when detecting fine seafloor topography (Wu et al., 2023).

Traditional satellite-altimetry-predicted depth and in situ data have been used to develop global bathymetry models, including the SRTM15 series ($15'' \times 15''$) (SRTM: Shuttle Radar Topography Mission) (Tozer et al., 2019) and Topo series of models ($1' \times 1'$) (https://topex.ucsd.edu/pub/global_topo_1min/, last access: 23 May 2025) provided by the Scripps Institution of Oceanography (SIO), the DTU series ($1' \times 1'$) (https://ftp.space.dtu.dk/pub/DTU18/1_MIN/, last access: 23 May 2025) developed by the Department of Space Research and Technology at Denmark Technical University (DTU Space), and the GEBCO (General Bathymetric Chart of the Oceans) series ($15'' \times 15''$) (https://www.gebco.net/data_and_products/gridded_bathymetry_data/, last access: 23 May 2025) compiled by the GEBCO Bathymetric Compilation Group. With the accumulation of bathymetric data and advancements in modeling, these models have achieved significant improvements in terms of spatial resolution and accuracy. However, owing to the scarcity of in situ data over shallow waters in the SCS, these models are limited in the accuracy of the bathymetric information, exhibiting data gaps, low spatial resolution, and high uncertainty for shallow-water areas (Wu et al., 2023). Consequently, the existing bathymetry models fail to deliver a unified, high-accuracy representation of the bathymetry in these areas.

In comparison, the Ice, Cloud, and land Elevation Satellite-2 (ICESat-2), equipped with the Advanced Topographic Laser Altimeter System (ATLAS), provides worldwide open-source water depths with an accuracy of 0.43–0.6 m and an along-track resolution of 0.7 m (Abdalati et al., 2010; Markus et al., 2017; Martino et al., 2019). Moreover, satellite-derived bathymetry (SDB) technology, utilizing satellite multispectral or hyperspectral imagery, provides comprehensive bathymetric data coverage (Albright and Glennie, 2020; Ma et al., 2020). SDB establishes the relationship between reflectance and water depth, and by combining ICESat-2 data with satellite imagery, SDB can be used to map shallow-water bathymetry with an accuracy of ~ 1 m and a resolution of a few meters (Hodúl et al., 2018; Jia et al., 2023; Ma et al., 2020). SDB utilizes openly available data and provides a rapid, accurate, and cost-effective way of capturing shallow-water depths with unparalleled accuracy and spatial resolution on a global scale, providing significant advantages over traditional approaches (Ferreira et al., 2022).

Given the lack of accurate water depths near island areas in the SCS, we focused on developing a high-quality shallow-water depth model with a unified spatial resolution using SDB by integrating ICESat-2 data with Sentinel-2 multispectral imagery. The model called HHU24SWDSCS represents a high-quality shallow-water-depth (SWD) model over the SCS developed by Hohai University in 2024. This model, which covers > 120 islands and reefs in the SCS,

is expected to serve as a potential substitute for existing bathymetry models in fields such as oceanography, geodesy, the environmental sciences, and marine production activities in the shallow waters of the SCS. The rest of this study is organized as follows: in Sect. 2, we introduce the study area and the data. Section 3 presents the principles for the preprocessing of the ICESat-2 data and for SDB estimation. Section 4 presents the modeling results and examines the model's performance, with validation against independent ICESat-2 and airborne lidar data. The performance of the latest global bathymetry models (DTU18BAT, topo_27.1, SRTM15 + V2.6, and GEBCO_2024) is evaluated and analyzed. Section 5 presents the conclusions.

2 Study area and data

The study area was the SCS (Fig. 1), with the latest high-resolution bathymetry model (GEBCO_2024, $15'' \times 15''$) providing the background bathymetry data (GEBCO Bathymetric Compilation Group 2024, 2024). The SCS, a marginal sea in the western Pacific Ocean (3–22° N, 105–120° E), is one of the most important maritime passages globally. Located in Southeast Asia, it covers $\sim 3.5 \times 10^6$ km^2, making it one of the largest and deepest marginal seas (> 5000 m deep in the Manila Trench) in the western Pacific Ocean (Wang et al., 2018a; Zhu et al., 2021). Over 100 islands and reefs are scattered across the SCS; these can be divided geographically into four archipelagoes: the Xisha islands, the Zhongsha islands, the Dongsha islands, and the Nansha islands. The latter account for > 70 % of the islands (Huang et al., 1994). The water depth around these islands and reefs is generally < 50 m, and their diameters range from 2 to 25 km (as depicted in Fig. 1). Conventional techniques, such as shipborne and airborne surveys, encounter numerous challenges in acquiring shallow-water depths over these islands across the SCS; this is particularly true for the Nansha islands, where political factors prohibit the use of in situ surveys for water depth measurements. However, the wide range of the ICESat-2 data and Sentinel-2 imagery provides a solid database for employing SDB to develop a shallow-water depth model covering these islands and reefs (Hsu et al., 2021; Ma et al., 2020). Since most of the Zhongsha islands comprise submerged shoals for which the ICESat-2 data do not provide valid seafloor topography information, this study focuses on SDB modeling over the Xisha, Dongsha, and Nansha islands (the geographical locations are displayed in the red boxes in Fig. 1a). As the Nansha islands are larger than the other two archipelagoes, they were divided into five subareas for results presentation, resulting in seven subareas in total, as shown in Fig. 1. Areas 1 and 2 cover the Xisha and Dongsha islands (Fig. 1b and c, respectively), and areas 3–7 comprise the Nansha islands (Fig. 1d–h). It is worth noting that the SDB modeling here is focused on shallow waters near islands and reefs, which is largely affected by the quality of ICESat-2 and Sentinel-2 multispectral data as well as by water quality, water conditions, and bottom types (Wu et al., 2023). Further information on the subareas is presented in Table 1.

Table 1. Description of selected subareas in the South China Sea (SCS).

Subarea	Latitude (° N)	Longitude (° E)	Number of islands or reefs
Area 1	15.75–17.15	111.15–112.80	36
Area 2	20.55–20.80	116.65–116.95	2
Area 3	9.68–11.53	113.80–115.35	49
Area 4	8.80–11.20	115.40–117.50	17
Area 5	8.05–9.75	111.60–113.40	6
Area 6	6.90–9.00	113.55–115.30	15
Area 7	4.95–5.60	112.50–112.65	3

2.1 ICESat-2 data

ICESat-2, launched by NASA in September 2018, has a revisit cycle of ca. 91 d and enables continuous monitoring of changes in Earth's surface. ICESat-2 is equipped with the latest ATLAS, which emits laser pulses at a 10 kHz pulse repetition frequency in six beams, achieving an along-track resolution of ∼ 0.7 m and a ranging accuracy of better than 1 m (Markus et al., 2017; Martino et al., 2019). It is capable of penetrating at depths > 30 m below the sea surface in clean waters and can measure bathymetry in shallow waters (Guo et al., 2022). For SDB modeling, we utilized the ICESat-2 Level-2A (L2A) Global Geolocated Photon Data (ATL03) V006 data product (https://www.earthdata.nasa.gov/, last access: 23 May 2025), in which each photon contains information such as latitude, longitude, along-track distance, off-nadir angle, data quality, elevation, and geophysical corrections for factors including solid Earth tides, ocean pole tides, and atmospheric delays (Neumann et al., 2021).

We utilized ICESat-2 data for 2018–2024, encompassing 512 tracks for the Xisha islands, 73 tracks for the Dongsha islands, and 1038 tracks for the Nansha islands, for a total of 1623 tracks with a maximum depth of approximately 30 m. Owing to the difficulty in obtaining in situ water depths (e.g., multibeam sounding data) around islands and reefs, the ICESat-2 data are used to both train and validate the SDB model. The training and validation sample sizes are selected by ensuring that the spatial distribution of both the training and validation data is uniform. This not only allows for better data control but also ensures good spatial coverage for the validation data. The ratios of the ICESat-2 data used for the training and validation data are approximately 80 % and 20%, respectively. The training (red tracks) and validation data (green tracks) over the seven subareas are illustrated in Fig. 2. Notably, the ICESat-2 data are acquired independently using individual beams, and hence the tracks do not

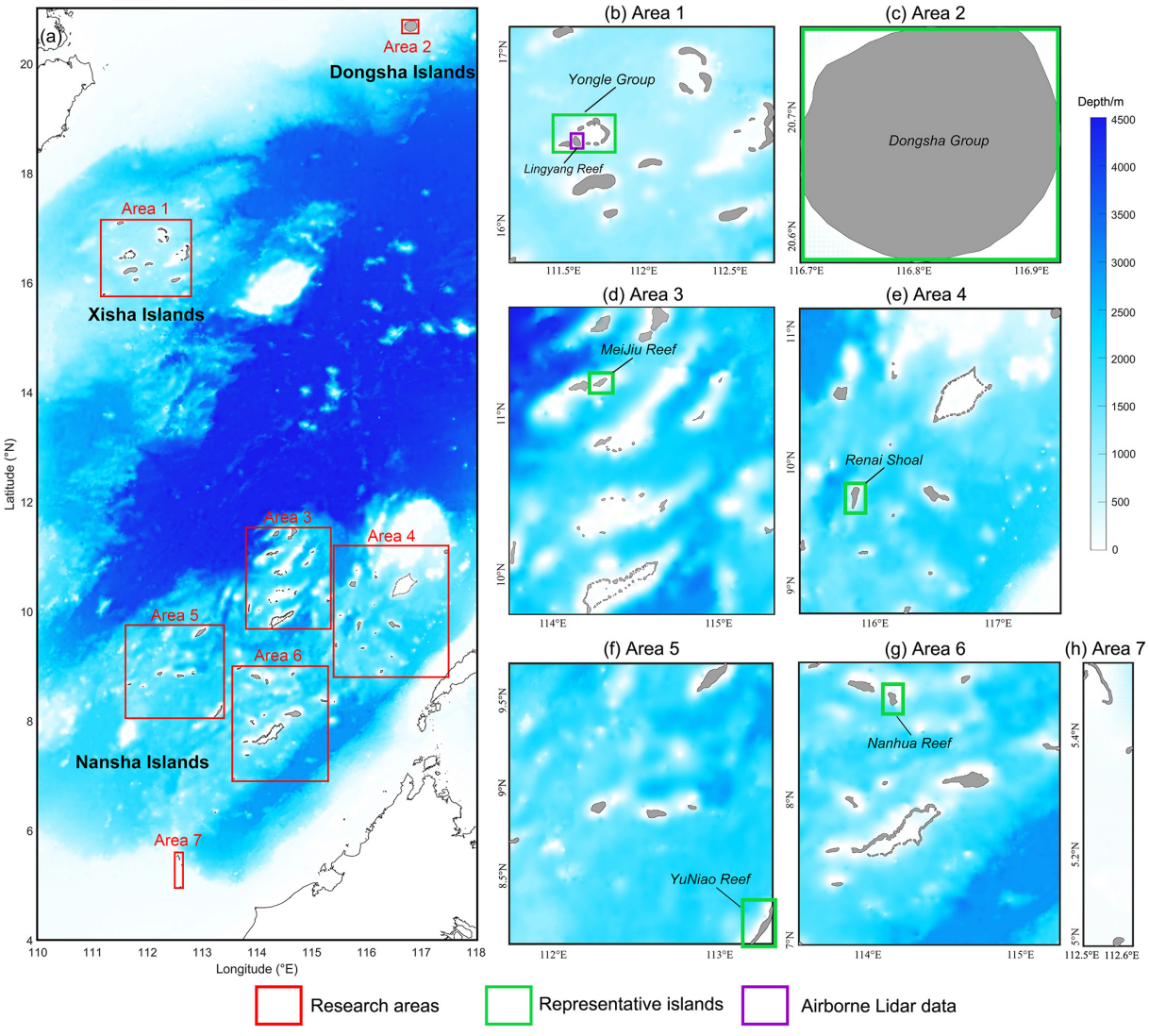

Figure 1. **(a)** Distribution of the islands and reefs over the South China Sea (SCS), and the seven areas in the red boxes display the subareas. Panels **(b)**–(h) represent Areas 1–7, respectively. The purple box in panel **(b)** displays the locations of the airborne lidar data in the Lingyang Reef over the Xisha islands. The six green boxes in panels **(b)**–**(g)** show the representative islands. The GEBCO_2024 model is used as a background.

influence one another and are not correlated. This ensures that the training data remain entirely independent of the validation data, allowing for objective assessment of the quality of the computed SDB data.

2.2 Sentinel-2 multispectral imagery

High-resolution multispectral imagery from the Sentinel-2A and Sentinel-2B L2A products provided by the European Space Agency (ESA) was utilized for SDB modeling. Sentinel-2A and Sentinel-2B were launched by the European Space Agency in June 2015 and March 2017, respectively (Drusch et al., 2012). Each carries a multispectral instrument and can capture 13 different spectral bands at 443–2190 nm, including blue, green, red, near-infrared, red-edge, and shortwave infrared bands. Their spatial resolution is 10 m, with a swath width of 290 km and a revisit period of 5 d (Gatti and Bertolini, 2015). Owing to its high spatial resolution and short revisit interval, the Sentinel-2 imagery is suitable for SDB modeling. In addition, the L2A products have been atmospherically corrected, offering surface reflectance for SDB modeling.

Here, the spectral information from the red, green, and blue bands was extracted from the Sentinel-2 multiband imagery, based on our preliminary finding that using these three bands yielded better results than using other combinations (Wu et al., 2023). To reduce the effects of temporal changes on bathymetry estimation, only images within the time span

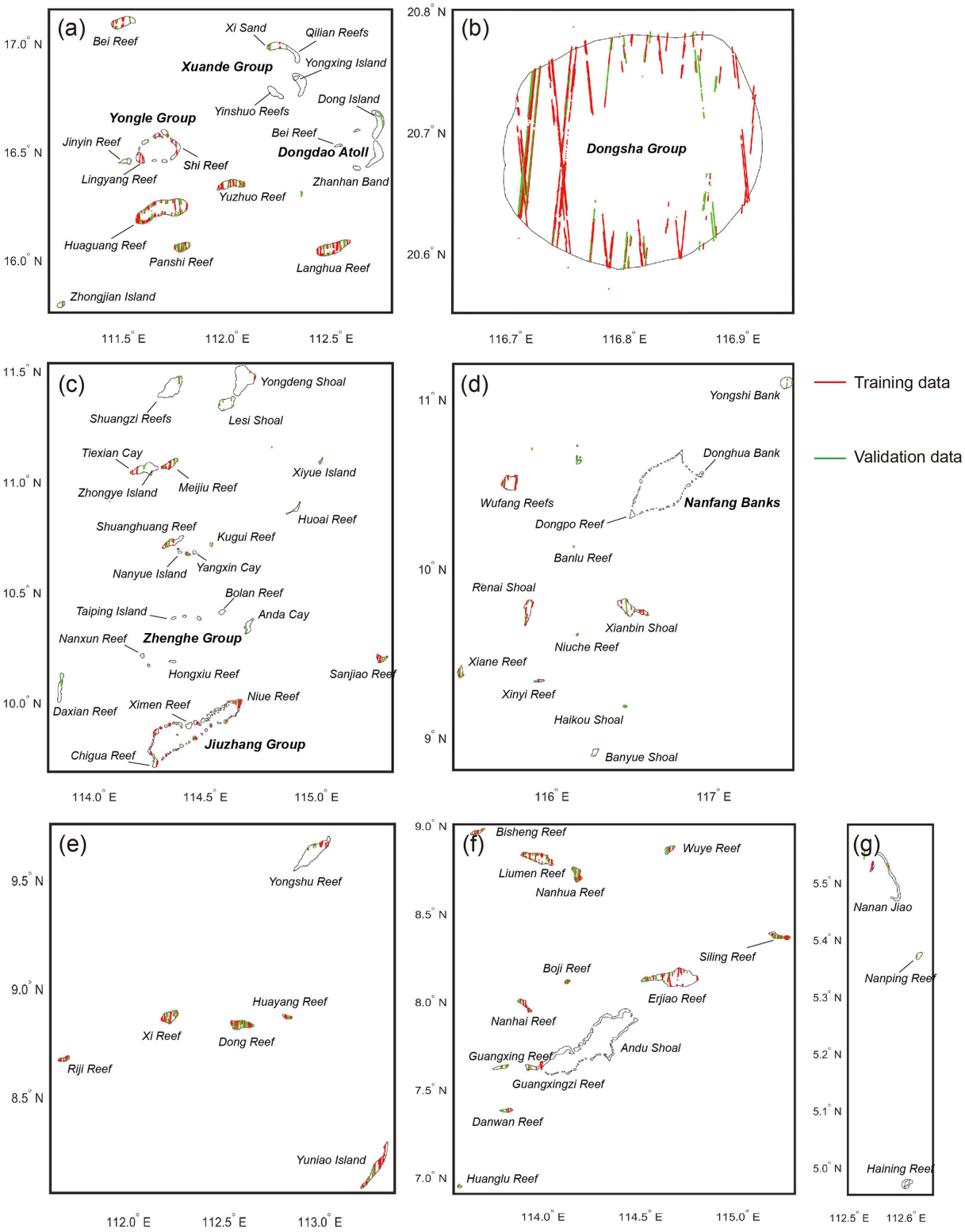

Figure 2. Distribution of the ICESat-2 training tracks (red) and validation tracks (green) over the seven subareas (**a–g**).

of the ICESat-2 data were selected (Wu et al., 2023, 2025). The AI EARTH platform (https://engine-aiearth.aliyun.com, last access: 23 May 2025) was used to select images with minimal cloud cover and Sun glint; 70 images were chosen, including 5 for the Xisha islands, 1 for the Dongsha islands, and 64 for the Nansha islands. Given that Sentinel-2 multispectral imagery is subject to various environmental interferences, including Sun glint, cloud cover, and image noise, coupled with substantial variations in water quality and seafloor composition across different island regions, this study performs separate modeling for each individual island or adjacent islands (e.g., Fig. 3a). This choice is based on the premise that external influencing factors maintain relative consistency within smaller geographical units, consequently minimizing their potential impact on the accuracy of the SDB results.

To assess the efficacy and applicability of the SDB modeling approach, six representative reefs with diverse geographical distributions, topographical features, and hydrological conditions were selected for presentation (Table 2). Figure 3 depicts the representative islands and reefs highlighted in the green boxes in Fig. 1, i.e., the Yongle Group (Area 1), the Dongsha Group (Area 2), the Meijiu Reef (Area 3), the Renai Reef (Area 4), the Yuniao Reef (Area 5), and the Nanhua Reef (Area 6). Figure 3 presents multispectral images (synthesized from the blue, green, and red bands), ICESat-2 water depth, and shallow-water masks (white polygons), along with preselected deep-water areas (purple box). The SDB modeling is conducted within the shallow-water masks of each reef. Notably, the GEBCO_2024 model is employed to identify and remove deep-water effects (> 100 m) in SDB estimation. The elimination of deep-water effects is intended to reduce Sun glint interference and reflection energy from the water body, which in turn helps to establish a more accurate relationship between seafloor reflection energy and water depth (Jia et al., 2023).

To obtain a precise shallow-water mask for a specific island, we first use the normalized difference water index (NDWI) in Sentinel-2 imagery to extract a raw mask, where the green and near-infrared bands are utilized to compute the NDWI (Gao, 1996). However, the performance of the NDWI in water mask identification is affected by the bottom type and water turbidity, which may lead to misclassification issues (Kirby et al., 2024; Yang et al., 2017b), and we further use the valid ICESat-2 seafloor topography information to correct and refine the initial water mask obtained from the NDWI. Sentinel-2 pixels exhibiting valid bathymetric signals from ICESat-2 were classified as shallow-water areas. This refined classification was then incorporated into the water mask, allowing for subsequent data screening and quality control.

2.3 Airborne lidar bathymetry

We used airborne lidar bathymetric data, provided by the Shanghai Institute of Optics and Fine Mechanics (SIOFM), to independently validate the SDB modeling results (Li et al., 2022; Yang et al., 2022). The airborne lidar system (Mapper5000) features a dual-frequency design, including a 1064 nm near-infrared surface channel and a 532 nm green channel for shallow and deep-water detection, with a pulse repetition frequency of 5 kHz. Operated at a flight altitude of 300 to 1100 m and a flight speed of 150 to 220 km h^{-1}, this system ensures efficient and accurate data collection. The raw data were preprocessed by SIOFM using procedures including waveform peak detection and range determination, overlapping waveform decomposition, and range-difference correction, based on proprietary algorithms (Yang et al., 2022). The accuracy of the airborne lidar water depth data for the Lingyang Reef is ~ 20 cm (Li et al., 2022). As illustrated in Fig. 4a, the lidar data cover the northwestern region of the Lingyang Reef in the Yongle Group, with water depths of 0–5 m and an effective point-cloud size exceeding 440 000 points.

2.4 Global bathymetry models

The recently released bathymetry models, including DTU18BAT (DTU Space, https://ftp.space.dtu.dk/pub/DTU18/1_MIN/, last access: 23 May 2025), topo_27.1 (https://topex.ucsd.edu/pub/global_topo_1min/, last access: 23 May 2025), SRTM15 + V2.6 (SIO, https://topex.ucsd.edu/pub/srtm15_plus/, last access: 23 May 2025), and GEBCO_2024 (GEBCO Bathymetric Compilation Group, https://www.gebco.net/data_and_products/gridded_bathymetry_data/, last access: 23 May 2025), were introduced for validation and analysis. DTU18BAT was developed by DTU Space in 2019, integrating the GEBCO dataset with satellite altimetric gravity anomalies (Andersen and Knudsen, 2008). It incorporates 3 years of Sentinel-3A data and 7 years of CryoSat-2 observations, offering a spatial resolution of $1'$. The topo_27.1 model, released by the SIO, also provides bathymetry at a spatial resolution of $1'$ (Sandwell et al., 2014). Derived from ship soundings and satellite altimetric gravity anomalies, this model continues the tradition of progressively refined seabed topography representations. SRTM15 + V2.6, updated by the SIO, features a finer spatial resolution of $15''$ (Tozer et al., 2019). This model combines shipboard soundings with satellite altimetric gravity data to provide an enhanced depiction of seafloor topography, reflecting a comprehensive analysis of available datasets. GEBCO_2024, the recent edition of the GEBCO series, builds on SRTM15 + V2.5.5 as its foundational dataset (Weatherall et al., 2015). Enhanced with in situ measurements such as echo soundings, seismic records, and lidar, the GEBCO_2024 model offers interpolated satellite-altimetry-predicted depths in areas lacking direct

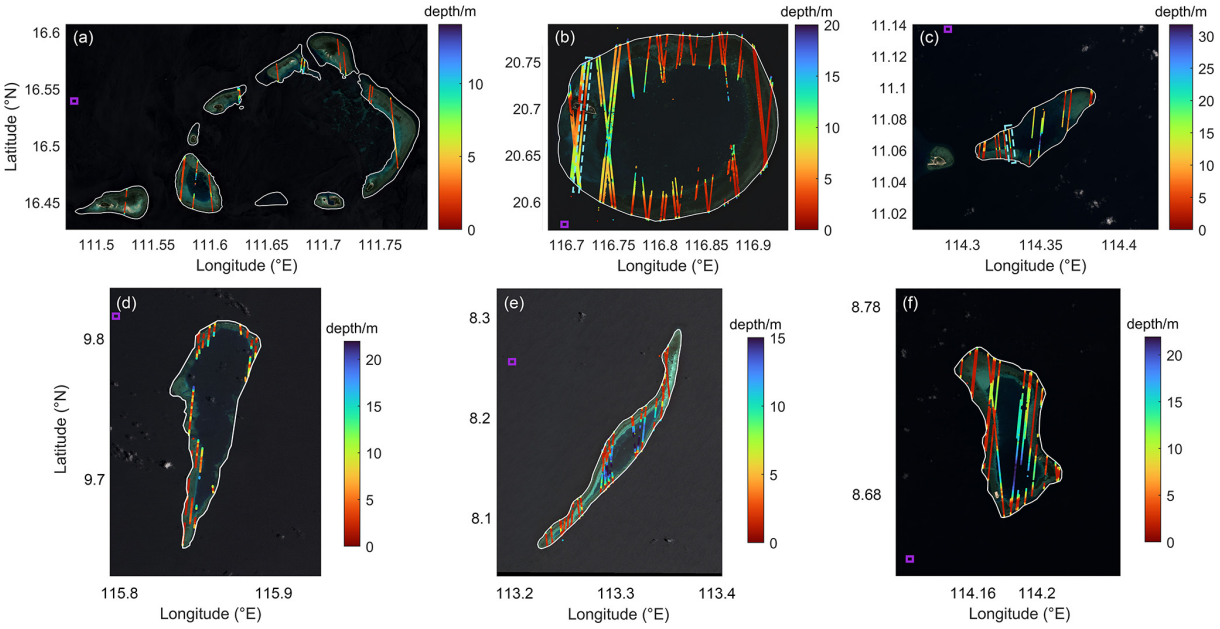

Figure 3. Representative islands in the research area. **(a)** Yongle Group, **(b)** Dongsha Group, **(c)** Meijiu Reef, **(d)** Renai Reef, **(e)** Yuniao Reef, and **(f)** Nanhua Reef. The white polygon denotes the shallow-water mask, the tracks indicate the ICESat-2 water depth data, the purple boxes indicate the reference deep-water areas, and the cyan dotted boxes in panels **(b)** and **(c)** indicate the typical nighttime and daytime ICESat-2 tracks shown in Figs. 6 and 7, respectively. The background images are synthesized from the Sentinel-2 red, green, and blue bands.

Table 2. Information on the representative islands.

Island name	Latitude (° N)	Longitude (° E)	ICESat-2 tracks	Sentinel-2 image
Yongle Group	16.43–16.60	111.48–111.79	19	20210817T025549
Dongsha Group	20.55–20.80	116.65–116.95	73	20230207T023901
Meijiu Reef	11.05–11.10	114.30–114.39	15	20240207T023859
Renai Reef	9.65–9.8	115.83–115.90	10	20240323T023531
Yuniao Reef	8.05–8.30	113.20–113.37	25	20200327T024541
Nanhua Reef	8.66–8.76	114.15–114.21	26	20190228T023631

measurements. Representing the pinnacle of global seafloor terrain depiction, it embodies an advanced understanding of underwater topography. Notably, these models have been interpolated to align with the SDB models, facilitating accurate comparisons and analyses.

3 Methodology

To perform SDB modeling for shallow-water regions of a specific island area, ICESat-2 data are first extracted using a shallow-water mask, followed by classification, denoising, refraction correction, and reference datum unification, to obtain high-precision shallow-water depth information. Then, the reflectance information within the shallow-water mask is extracted from the optimal Sentinel-2 image, and a reference deep-water correction is applied to reduce the Sun glint effect. Subsequently, the extracted reflectance information is matched with the processed ICESat-2 depth information, and a Pearson correlation analysis is performed to reduce anomalous data. Based on a multivariate linear band model (LBM), regression training is performed using all ICESat-2 depth training data and their corresponding reflectances to solve for the regression parameters. Finally, the SDB estimation is derived based on the reflectance data of the shallow-water area and the LBM.

3.1 ICESat-2 data preprocessing

To obtain effective bathymetric data from the ICESat-2 point cloud, this study adopts a sea surface and seafloor identification method based on the point-cloud density distribution (Hsu et al., 2021). This involves noise removal, point-cloud density estimation, sea surface identification, and water depth point-cloud extraction. Refraction corrections and reference datum unifications are then applied to derive accurate water depth measurements.

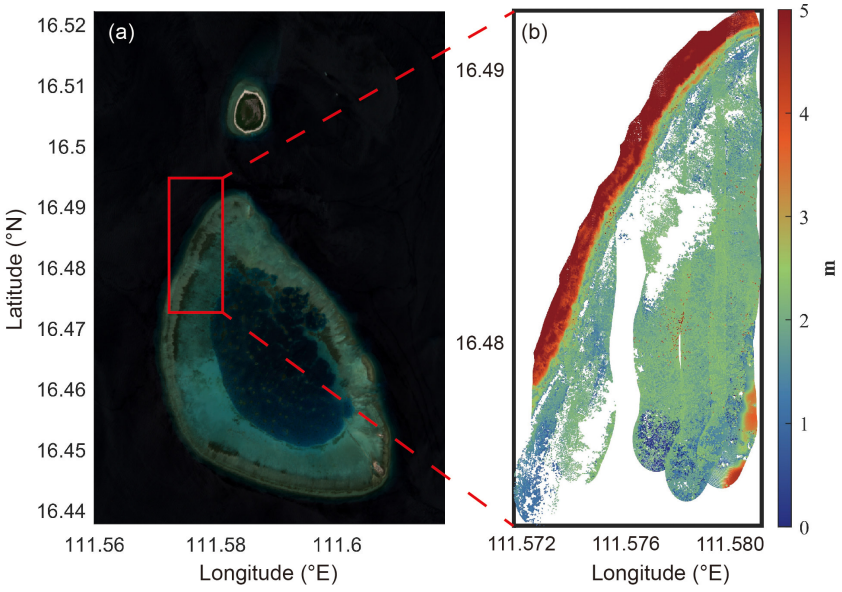

Figure 4. **(a)** The Sentinel-2 image of the Lingyang Reef and the distribution of the airborne lidar data. **(b)** The zoomed-in view of the airborne lidar water depth data.

3.1.1 Sea surface identification

We propose a method for sea surface identification based on the anisotropic point-cloud density. First, considering the distribution characteristics of the sea surface and bathymetric point data, an elliptical sliding window is constructed to capture their geometric profiles. For each photon $p_i = (x_i, y_i), i = 1, \ldots, N$, an elliptical window is established at p_i, and the number of point data within the elliptical window is derived:

$$\begin{aligned} d_{ij} &= \sqrt{\left(\frac{x_j - x_i}{a}\right)^2 + \left(\frac{y_j - y_i}{b}\right)^2}, \\ D_i &= \{j | d_{ij} \le 1, j = 1, \ldots, N, j \ne i\}, \end{aligned} \tag{1}$$

where $a = 50$ and $b = 2$ m denote the major and minor axes of the elliptical window; d_{ij} represents the distance of p_j relative to the ellipse; D_i is the number of points within the elliptical window centered at p_i; N is the total number of point data; and x_i, y_i represent the along-track distance and point-cloud elevation, respectively.

For each point, the number of point data within the elliptical neighborhood is computed, normalized, and used as the point-cloud density distribution:

$$\rho(x_i) = \frac{D_i - \min(\boldsymbol{D})}{\max(\boldsymbol{D}) - \min(\boldsymbol{D})}, \tag{2}$$

where ρ denotes the point-cloud density map and $\boldsymbol{D}$ represents the vector of the number of neighboring point data for each point.

Subsequently, the statistical analysis based on Scott's rule is performed to estimate the noise threshold (Scott, 1979), as follows:

$$T_{\text{noise}} = \frac{3.5 \cdot \sigma}{\sqrt[3]{N}}, \tag{3}$$

where σ represents the standard deviation of ρ. Point data exceeding the noise threshold are removed.

Next, the point-cloud density map is discretized into a grid with a cell resolution of 0.5 m in elevation and an along-track resolution of 30 m. This density grid is then stacked in the along-track direction to accumulate the density for each elevation cell. By calculating the gradient of the accumulated density, we identify the elevations corresponding to the maximum and minimum gradient values, thereby locating the boundary of the sea surface point cloud. Consequently, the point data within this boundary are extracted and fitted to estimate the sea surface height (SSH). This is then used as the instantaneous SSH at the time of the ICESat-2 measurement.

3.1.2 Bathymetry point-cloud extraction

After removing the detected sea surface point cloud, the density grid of the remaining point cloud and the noise threshold are recalculated, and point data exceeding 0.5 times the noise threshold are removed. To more accurately extract the bathymetry information, the maximum density points are identified along the depth direction, and the point cloud within ± 1 m of the maximum density point is marked as the bathymetry point cloud. Considering the measurement accuracy of ± 1 m in the ICESat-2 bathymetry data, a local weighted least-squares (LS) fitting algorithm is used to extract the bathymetry.

3.1.3 Refraction correction

Refraction is one of the most significant factors influencing the accuracy of ICESat-2 laser bathymetry (Yang et al., 2017a), which is deduced by the different propagation speeds of light in different media (such as in air and seawater). In shallow-water areas, the refraction effect is more pronounced, owing to the influence of sea surface waves and the resulting change in depth. We initially estimated shallow-water depths by computing the difference between the seafloor photon-derived depth and the corresponding sea surface height. However, considering the time difference between the acquired ICESat-2 and Sentinel-2 data used for modeling, a unified reference datum is required as the preliminary depth information. We therefore used the latest DTU22MSS model as the reference datum for bathymetric data correction (Wu et al., 2023).

Based on the solar zenith angle information ($\mathrm{ref_{elev}}$) in the ICESat-2 ATL03 product, the photon incidence angle (θ_1) can be expressed as follows (Ma et al., 2020):

$$\theta_1 = \frac{\pi}{2} - \mathrm{ref_{elev}}. \tag{4}$$

Based on Snell's law of refraction, the refraction angle (θ_2) is derived:

$$\theta_2 = \sin^{-1}\left(\frac{n_1 \sin\theta_1}{n_2}\right), \tag{5}$$

where $n_1 = 1.00029$ and $n_2 = 1.34116$ denote the refractive indices of air and water, respectively.

Considering the change in their propagation path when photons travel through water, the path length can be expressed as follows:

$$\begin{aligned} S_1 &= \tfrac{Z_0}{\cos\theta_1}, \\ S_2 &= \tfrac{S_1 n_1}{n_2}, \end{aligned} \tag{6}$$

where S_1 and S_2 represent the underwater path lengths of a photon before and after considering the refractive effect, and Z_0 is the water depth before refraction correction.

Therefore, the difference in photon position owing to refraction (P) can be obtained as follows:

$$\begin{aligned} P &= \sqrt{S_2^2 + S_1^2 - 2S_2 S_1 \cos\varphi}, \\ \varphi &= (\theta_1 - \theta_2). \end{aligned} \tag{7}$$

Consequently, the difference in the along-track direction (Δx) and elevational direction (Δd) due to refraction can be expressed as follows.

$$\begin{cases} \Delta x = P\cos\beta \\ \Delta d = P\sin\beta \\ \beta = \frac{\pi}{2} - \theta_1 - \alpha \\ \alpha = \sin^{-1}\left(\frac{S_2 \sin\varphi}{P}\right) \end{cases} \tag{8}$$

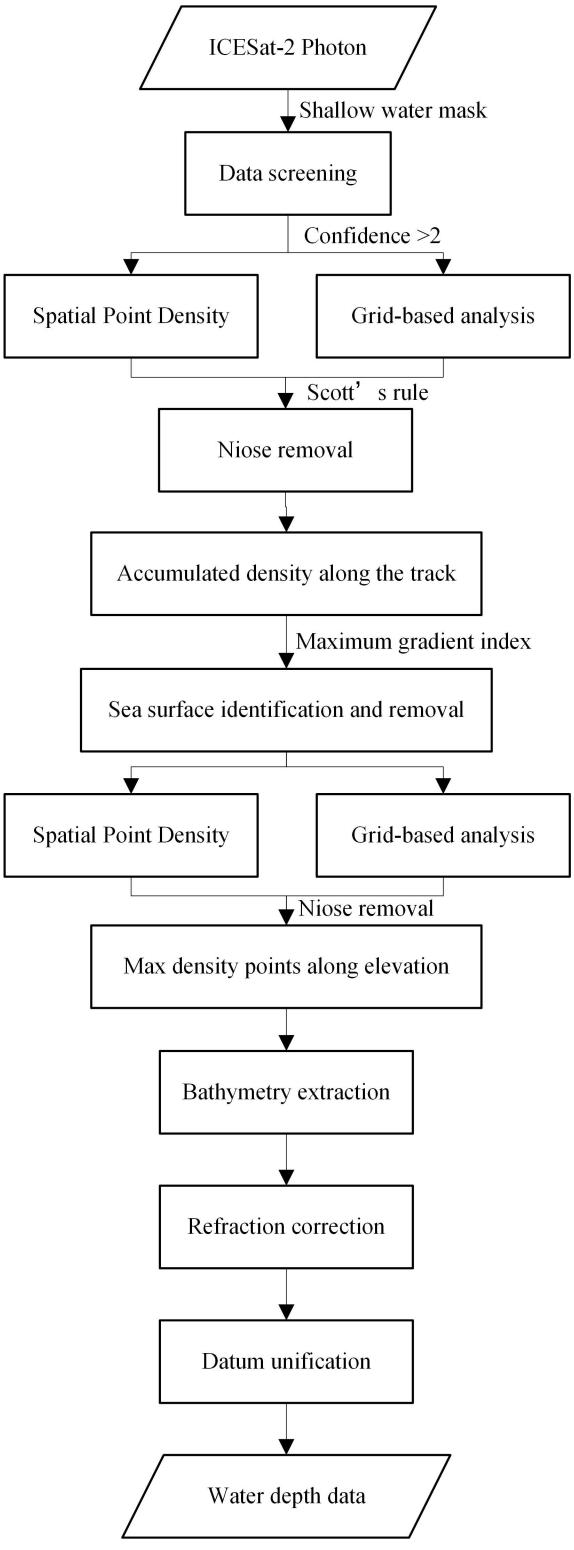

Figure 5. Flowchart for ICESat-2 water depth extraction.

The datum of water depth is then referenced to the DTU21MSS datum (Wu et al., 2023), as follows:

$$Z_{\mathrm{depth}} = h_{\mathrm{MSSH}} - Z_{\mathrm{sentinel}} + Z_0 + \Delta d - h_b + \Delta h, \tag{9}$$

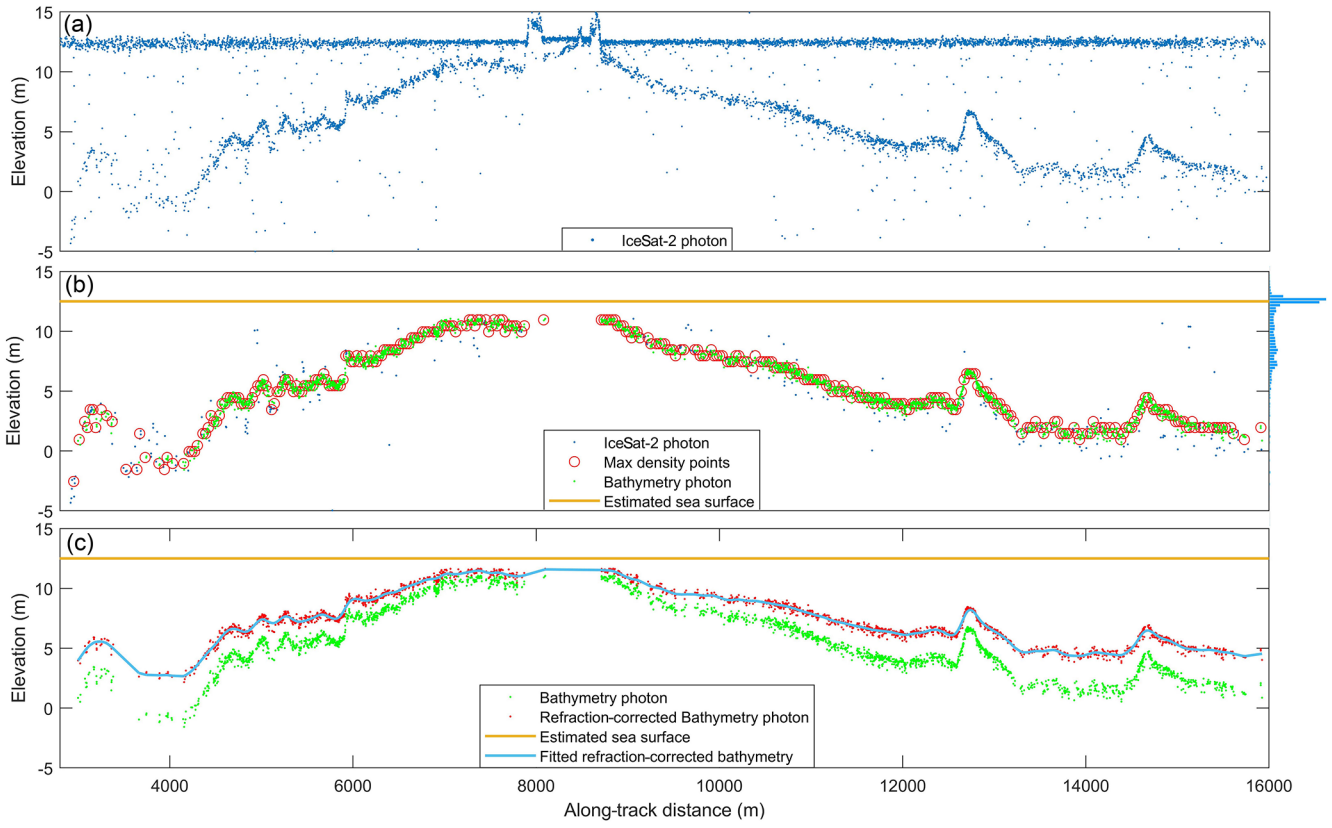

Figure 6. **(a)** Raw ICESat-2 photons. **(b)** Noise removal, sea surface identification, and water depth extraction. **(c)** Refraction correction for the ICESat-2 track in the Dongsha Group (nighttime) as shown in Fig. 3b.

where h_{MSSH} is the mean sea surface height (MSSH) obtained from the DTU21MSS model, Z_{sentinel} is the SSH at the Sentinel-2 imaging time, Z_0 is the ellipsoidal height of a sea surface photon, h_b is the ellipsoidal height of an underwater photon, and Δh is the difference between the SSH at the Sentinel-2 imaging time and the SSH at the ICESat-2 data acquisition time. The ICESat-2 preprocessing algorithm is illustrated in Fig. 5.

Using this protocol, the raw ICESat-2 photons were preprocessed. Two representative samples, over the Dongsha Group and the Meijiu Reef, represented by the cyan dotted boxes in Fig. 3b and c, respectively, are illustrated (Fig. 6). The data acquisition time of the ICESat-2 track for the Dongsha Group was 22:41 (nighttime) on 29 January 2019. Photons representing sea surface and bathymetry information can be clearly distinguished, as both are continuously distributed along the track direction. Notably, only photons with confidence levels of 3 and 4 were used in bathymetric information extraction (Neumann et al., 2021). The sea surface is smooth over the study area, and the photons are distributed within ± 1 m of the sea surface. In contrast, the distribution of the seafloor point cloud is irregular. Figure 6a depicts the raw ICESat-2 photon data and Fig. 6b the results of denoising and identification of the sea surface and seafloor point clouds. Following noise threshold estimation and point-cloud removal, the noise in the point-cloud data was effectively suppressed. The bar chart (Fig. 6b, right panel) displays the cumulative along-track density. The point-cloud density was higher at the sea surface than below the surface, and the cumulative along-track point-cloud density exhibited notable peaks. Based on the proposed approach, the sea surface point data were identified accurately (yellow lines, Fig. 6b). Moreover, the bathymetry point data (green points, Fig. 6b) were identified by locating the areas with the highest elevational point density (red circles, Fig. 6b). Finally, the seafloor was identified via local least-squares fitting. The red scatter points and the blue line in Fig. 6c represent the refraction-correction results and the fitted seafloor, respectively.

In comparison, the ICESat-2 track for the Meijiu Reef (Fig. 7) was acquired at 15:26 (daytime) on 9 March 2020. Relative to the nighttime results (Fig. 6a), the daytime results exhibit more noise in the raw ICESat-2 photon data (Fig. 7a) due to the greater illumination effects during the day, which presents challenges for water depth detection. For instance, as shown in Fig. 7b, a significant number of noise-related point clouds remained after denoising (e.g., at an along-track distance of ~ 500 m), although the proposed algorithm effectively identifies the along-track water depth point cloud

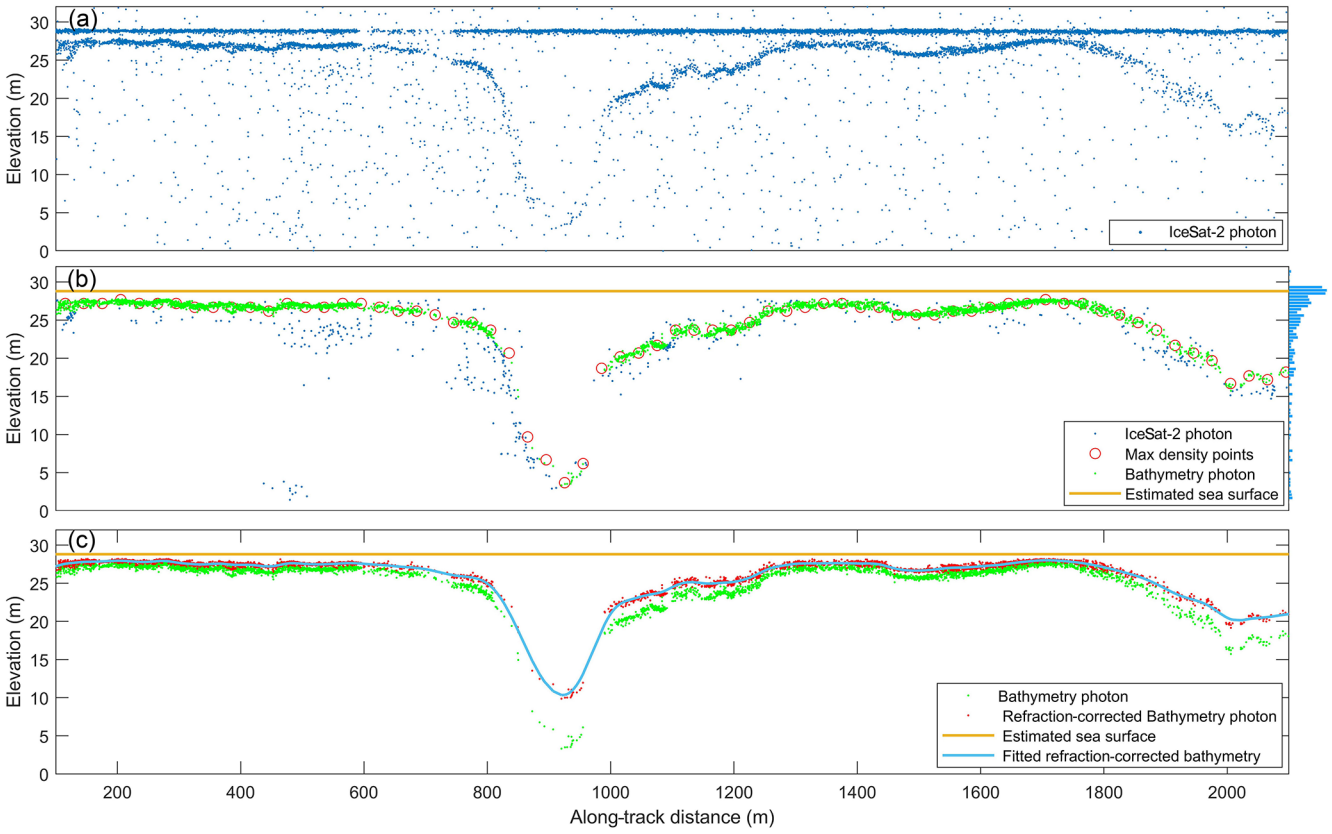

Figure 7. **(a)** Raw ICESat-2 photons. **(b)** Noise removal, sea surface identification, and water depth extraction. **(c)** Refraction correction for the ICESat-2 track in the Meijiu Reef (daytime) shown in Fig. 3c.

(highlighted by the red circle in Fig. 7b) and, via a function fitting, achieves robust extraction of the seafloor. The red scatter points and the blue line in Fig. 7c represent the refraction-correction results and the fitted water depth.

3.2 SDB modeling methodology

SDB was modeled by combining the ICESat-2 training data and Sentinel-2 multispectral imagery using the LBM, which achieves slightly better results than the band ratio model (Lyzenga et al., 2006; Thomas et al., 2021; Wu et al., 2023). SDB is modeled as follows:

$$H_{\mathrm{SDB}} = h_0 + \sum_{i=1}^{n} h_i \ln[R(\lambda_i) - R_\infty(\lambda_i)], \tag{10}$$

where H_{SDB} is the water depth derived from a multispectral image, $R(\lambda_i)$ represents the water surface reflectance of band i, n denotes the number of spectral bands used for SDB estimation, and $R_\infty(\lambda_i)$ is the average deep-water reflectance of band i. Parameters h_0 and h_i are the coefficients estimated via multiple linear regression, as follows:

$$\begin{cases} h_i = \dfrac{\sum_{i=1}^{n} x_i y_i - n\overline{x}\,\overline{y}}{\sum_{i=1}^{n} x_i^2 - n\overline{x}^2}, \\ h_0 = \overline{y} - h_i \overline{x}, \end{cases} \tag{11}$$

where $x_i = R(\lambda_i) - R_\infty(\lambda_i)$, y_i represents the depths obtained from the ICESat-2 training data, and $\overline{x}$ and $\overline{y}$ are the mean values of x_i and y_i, respectively.

Notably, to ensure robustness and generalizability, the h_i parameters are estimated by all ICESat-2 water depth training data within the shallow-water area of the reef.

The quality of the ICESat-2 data is affected by the water quality, seabed conditions, and inherent noises, which inevitably affects the SDB modeling. Prior to modeling the SDB data, a data-screening scheme based on correlation analysis was applied to eliminate anomalous and noisy data. The water depth data for each track were first divided into several segments based on the along-track distance (e.g., 500 m). For each segment, the Pearson correlation coefficient between the ICESat-2 depth and the reflectance of each specific band was calculated, as per Benesty et al. (2009):

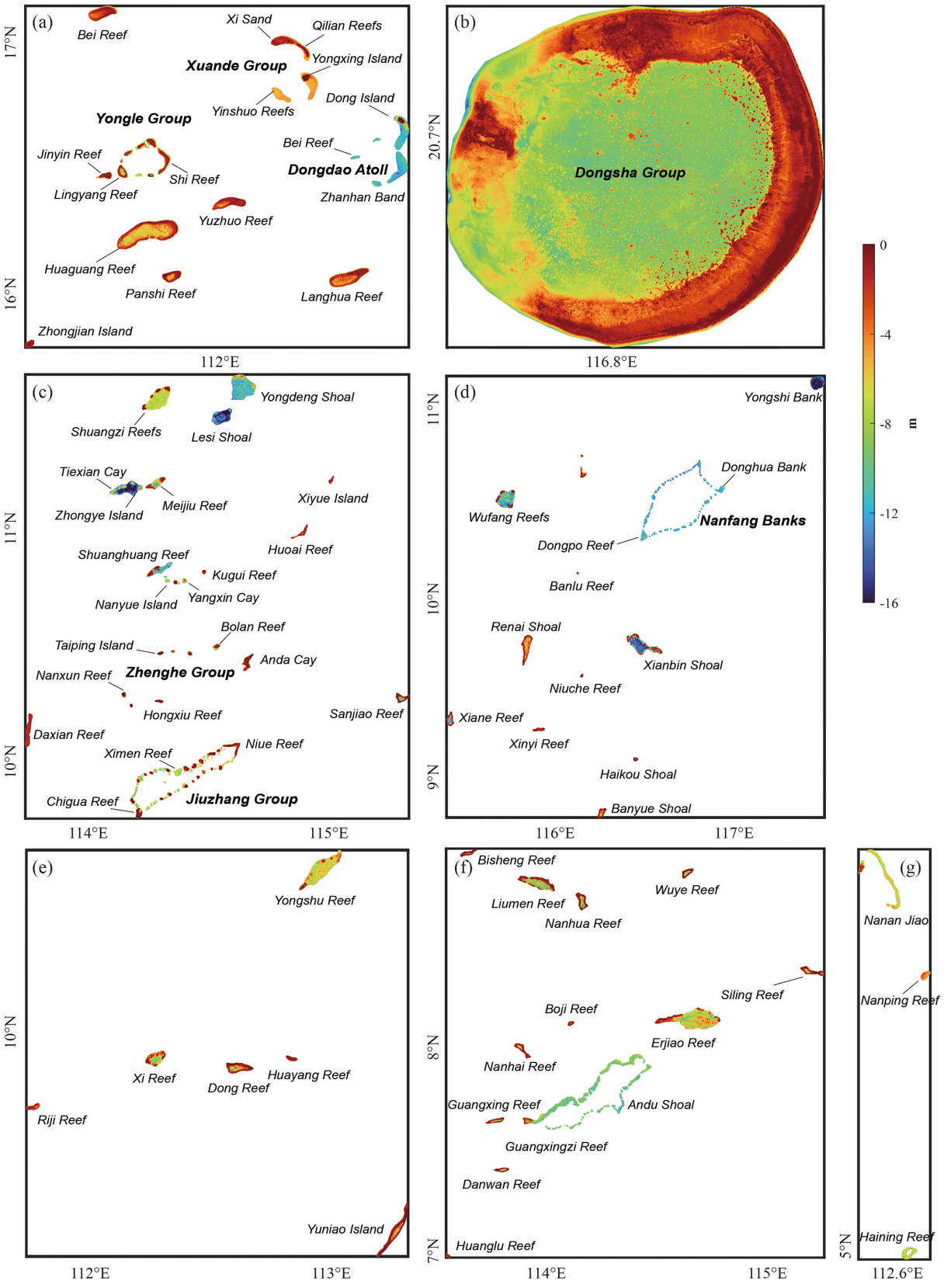

Figure 8. The SDB results in **(a)** Area 1, **(b)** Area 2, **(c)** Area 3, **(d)** Area 4, **(e)** Area 5, **(f)** Area 6, and **(g)** Area 7, respectively.

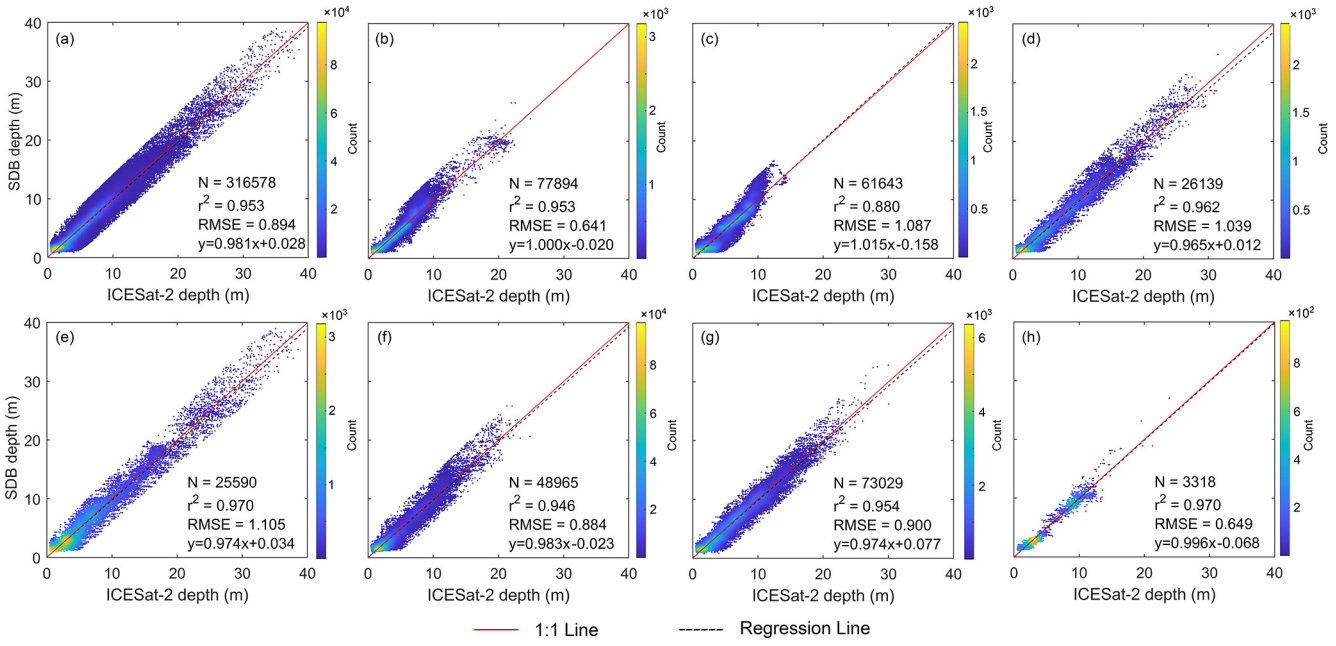

Figure 9. Training results of HHU24SWDSCS for **(a)** the entire SCS, **(b)** Area 1, **(c)** Area 2, **(d)** Area 3, **(e)** Area 4, **(f)** Area 5, **(g)** Area 6, and **(h)** Area 7, respectively. The red line represents the 1 : 1 line, and the black dashed line corresponds to the regression line.

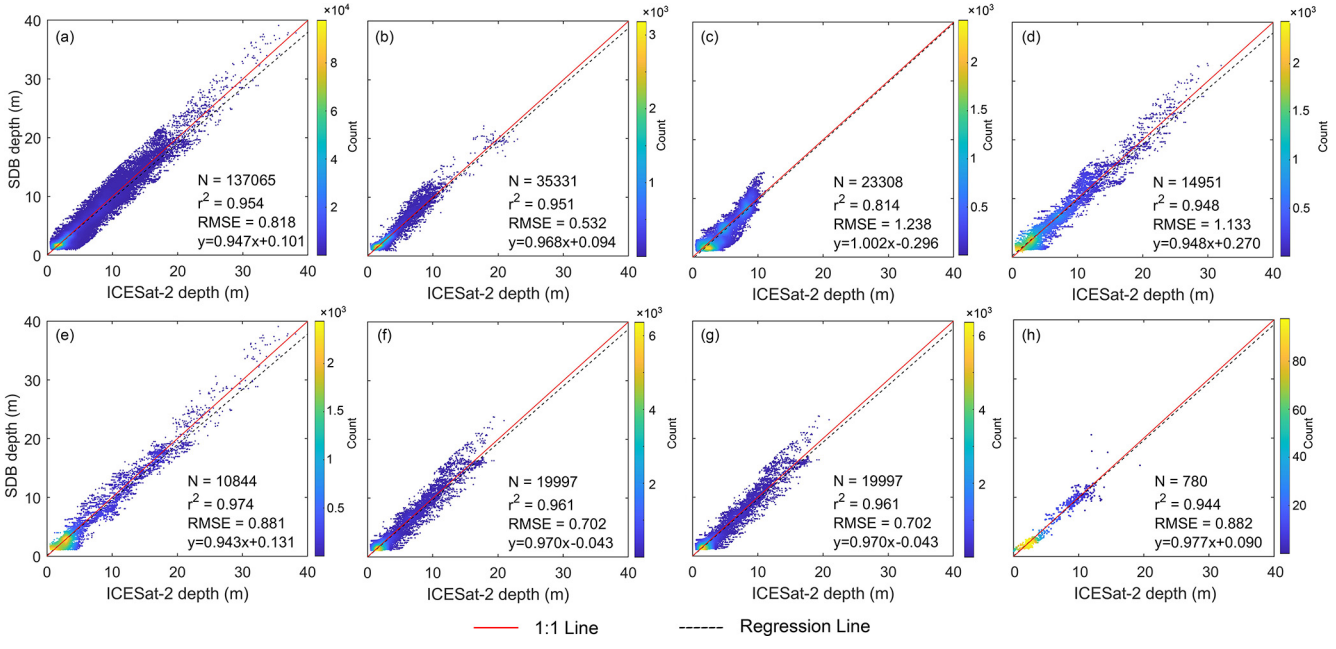

Figure 10. Validation results of HHU24SWDSCS for **(a)** the entire SCS, **(b)** Area 1, **(c)** Area 2, **(d)** Area 3, **(e)** Area 4, **(f)** Area 5, **(g)** Area 6, and **(h)** Area 7, respectively. The red line represents the 1 : 1 line, and the black dashed line corresponds to the regression line.

$$\rho(Z,R) = \frac{1}{N-1}\sum_{i=1}^{N}\left(\frac{Z_i-\mu_Z}{\sigma_Z}\right)\left(\frac{R_i-\mu_R}{\sigma_I}\right), \quad (12)$$

where ρ is the Pearson correlation coefficient; Z is the ICESat-2 depth; R is the reflectance; N is the number of ICESat-2 data points in this segment; μ_Z and σ_Z represent the mean and standard deviation of Z, respectively; and μ_R and σ_R denote the mean and standard deviation of R, respectively.

It is noted that the ICESat-2 data exhibit a higher resolution ($\sim$0.7 m along the track) than the Sentinel-2 imagery

(∼ 10 m). Before correlation analysis, bilinear interpolation was used to estimate reflectance at the locations of ICESat-2 photons. Correlation analysis was conducted track by track, and Pearson correlation coefficients were computed for all three visible bands, producing three correlation coefficients for each ICESat-2 photon. An ICESat-2 photon was excluded from SDB training if two or more of its correlation coefficients were smaller than a predetermined threshold (e.g., 0.4).

The deep-water radiative correction was implemented to effectively mitigate Sun glint and water column reflectance interferences, resulting in improved performance in the reflectance–depth relationship establishment (Jia et al., 2023; Wu et al., 2023). Additionally, the GEBCO_2024 model was used as a reference to select deep-water areas, where regions with depths exceeding 100 m are identified as deep waters (see the purple rectangles in Fig. 3). For a specific region, the training ICESat-2 data and the corresponding Sentinel-2 imagery were combined to establish a linear relationship between water depth and surface reflectance. Then, multiple linear regression analyses were performed to estimate the h_i coefficients in the LBM.

The root mean square error (RMSE) and the coefficient of determination (R^2) were used to evaluate the accuracy of the SDB data and the correlation between the predictions and the validation values, as follows:

$$\mathrm{RMSE} = \sqrt{\frac{1}{N}\sum_{i=1}^{N}(y_i - \hat{y}_i)^2},$$
$$R^2 = 1 - \frac{\sum_{i=1}^{N}(y_i - \hat{y}_i)^2}{\sum_{i=1}^{N}(y_i - \overline{y})^2}, \quad (13)$$

where y_i and $\hat{y}_i$ represent the ith estimated depth and the validation data, and $\overline{y}$ denotes the mean value.

While R^2 is redundant with RMSE, it has the additional characteristic of reflecting the correlation between the predictions and the validation values. Therefore, RMSE was used as the accuracy metric for the SDB model, and R^2 values are also included.

4 Results and discussion

4.1 SDB estimation

SDB modeling was performed using 1298 ICESat-2 shallow-water depth data tracks (2018–2024) and 70 Sentinel-2 images. Functional mapping between the training data and multispectral information was established within the shallow-water mask based on the linear band model approach, where three visible bands (B2, blue; B3, green; and B4, red) were used to train the LBM. The derived SDB model (HHU24SWDSCS) covers 128 islands and reefs in the SCS (Table A1).

Table 3. Statistics of the validation results between the bathymetry models against airborne lidar water depth data (m).

Model	Maximum	Minimum	Mean	RMSE
SDB	3.35	−4.14	−0.01	1.01
DTU18BAT	105.76	28.68	59.25	61.03
topo_27.1	66.67	−35.62	−14.01	25.03
SRTM15 + V2.6	23.93	−7.52	2.38	4.30
GEBCO_2024	58.68	25.33	32.16	32.38

Figure 8 illustrates the SDB results of HHU24SWDSCS, showing rich details of the seafloor topography. The SDB depth ranges from 0 to 30 m, capturing the typical morphology of coral reefs and sandbanks. In Area 1 (Xisha islands), it shows water depths ranging from 0 to 15 m. This area contains numerous ring-shaped coral reefs (e.g., the Yongle Group and the Huaguang Reef), and the seafloor topography is characterized by deeper central regions and shallower outer regions. In Area 2 (Dongsha islands), it indicates water depths ranging from 0 to 20 m. Around the outer coral ring reefs, the water depths range from 2 to 10 m, with a gradual deepening towards the west and shallowing towards the east. Within the inner waters, the average depth is ∼ 10 m, with the deepest point reaching 19 m. Areas 3–7 (Nansha islands) exhibit more diverse depth patterns. The islands and reefs in this region primarily comprise coral reefs and submerged shoals, which are typically small and scattered. The water depths are generally deeper than those in the Xisha islands and Dongsha islands, ranging from 0 to 30 m.

Figure 9 presents the SDB training results for the entire SCS (Fig. 9a) and for the seven subareas (Fig. 9b–h). Each subfigure includes annotations for the number of point data, the regression linear equation, as well as R^2 and RMSE. It is evident that the SDB results are highly consistent with the training data. Regression analysis of the training data for the entire SCS region yielded an RMSE of 0.89 m. The best performance was achieved for Area 1 (Fig. 9b), with an RMSE of 0.64 m. For all of the subareas, the RMSEs are below 1.1 m, i.e., $< 5\,\%$ of the maximum detectable water depth in the respective regions. These results reflect the high accuracy of the SDB in fitting this shallow-water bathymetry, with good model stability and robustness.

Figure 10 presents the SDB validation results for the entire SCS (Fig. 10a) and for the seven subareas (Fig. 10b–h). Notably, the ICESat-2 validation data used here were not introduced in the SDB modeling process, making them suitable for independent validation. The validation results (Fig. 10) reveal findings similar to the training results (Fig. 9). The validation results for the entire SCS yield an RMSE of 0.82 m and RMSEs from 0.53 to 1.24 m in the subregions. Comparison of Figs. 9 and 10 reveals that the training and validation

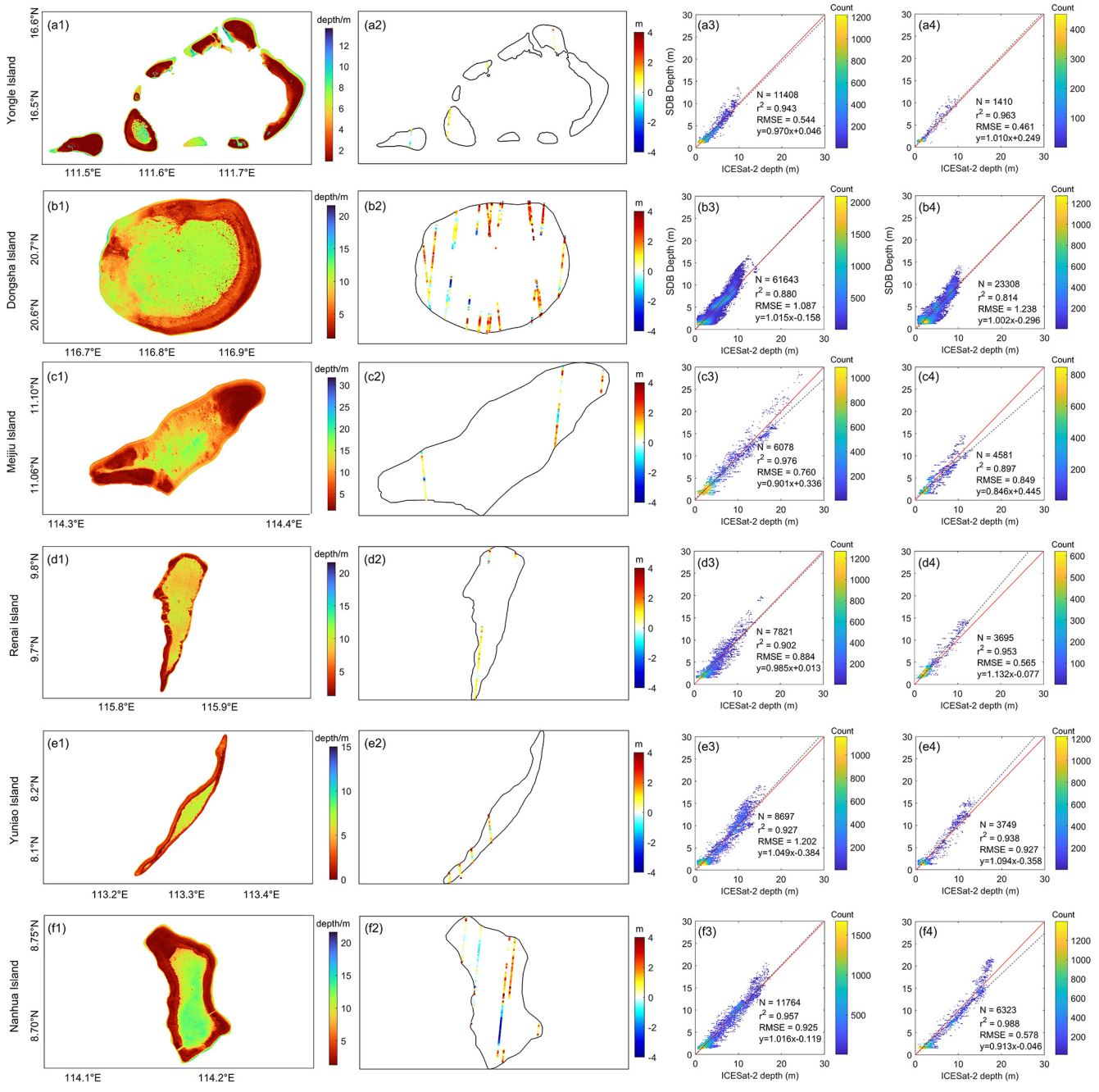

Figure 11. HHU24SWDSCS for the representative reefs (first column), the validation results using independent ICESat-2 water depth data (second column), the regression analysis between the SDB results and the training data (third column), and the validation data (fourth column).

RMSEs are highly consistent. Therefore, this SDB algorithm produces reasonable estimates, exhibiting strong generalization capability and the potential for model transfer.

To illustrate the details of the SDB bathymetry model, six representative reefs shown in Fig. 3 were selected for individual analysis. Figure 11 (Column 1) presents the SDB results of these representative islands and reefs, illustrating their geographical distributions, topographical features, and hydrological conditions. The Yongle Group, located in Area 1, comprises several reefs with diameters of ∼ 5 km and average water depths of ∼ 5 m (Fig. 11a1). In addition, the Lingyang Reef, located in the southwestern part of the Yongle Group, exhibits a typical central lagoon morphology characterized by deeper waters in the center and shallower waters along the edges. The Dongsha Group is located in Area 2, with diameters of over 20 km (Fig. 11b1). Known

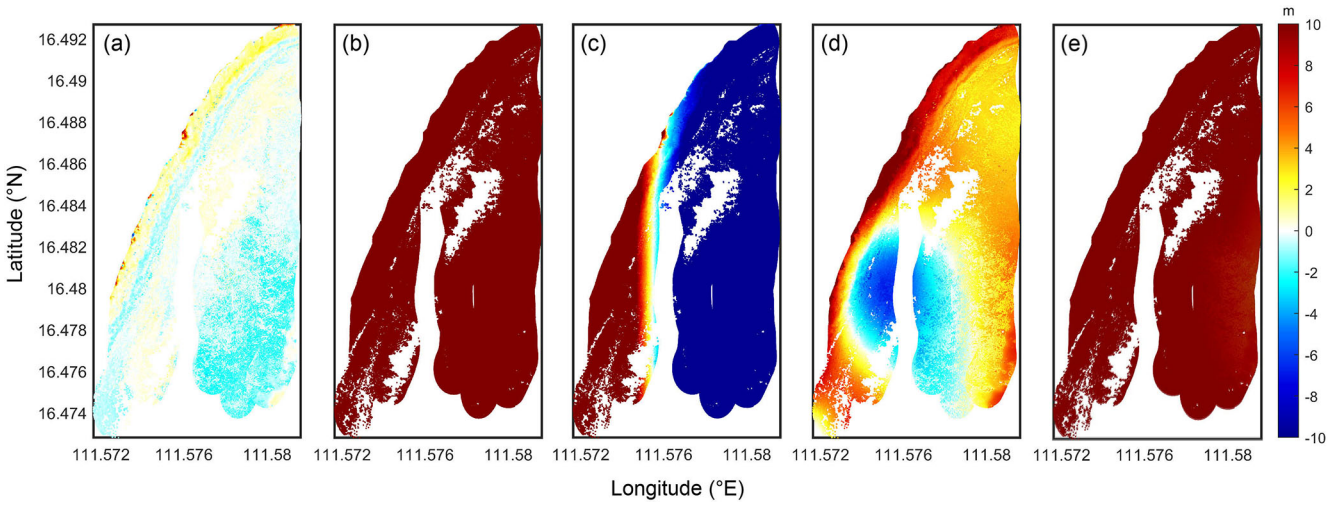

Figure 12. Validation of **(a)** HHU24SWDSCS, **(b)** DTU18BAT, **(c)** topo_27.1, **(d)** SRTM15 + V2.6, and **(e)** GEBCO_2024 against the surveyed airborne lidar water depth in the Lingyang Reef.

for their atoll structure, the Dongsha islands exhibit a distinct lagoon morphology, and the SDB model accurately captures complex bathymetric patterns, including the central lagoon (∼ 12 m) and the surrounding reef (∼ 3 m). The Meijiu Reef, located in Area 3, is a V-shaped reef spanning ∼ 9 km (Fig. 11c1), with coral reefs primarily in the northeastern and southwestern parts of the islands (∼ 3 to 5 m deep) and a central lagoon (up to 20 m deep). Additionally, the SDB model in Fig. 11c1 clearly reveals the complex underwater terrain, including water channels on the western and southwestern sides of the reef. The Renai Reef, located in Area 4, is a narrow, elongated north–south reef (Fig. 11d1); the SDB successfully reveals the narrow passages at the reef's edge and the sharp transitions between the reef flats and the lagoon. The Yuniao Reef, located in Area 5, is even narrower and more elongated in a northeast–southwest orientation, with its narrowest point being just 1.2 km, presenting a challenge for retrieving effective ICESat-2 water depth data (Fig. 11e1). Nonetheless, the SDB model yields reasonable results for this reef, revealing a central lagoon depth of ∼ 8 m and an edge depth of ∼ 4 m. Finally, for the Nanhua Reef (located in Area 6), the SDB results (Fig. 11f1) successfully reveal two water channels approximately 100 m wide in the southwestern and eastern parts of the reef.

Based on the SDB validation results (Fig. 11, Column 2), most of the discrepancies between the SDB and the ICESat-2 validation data are within ±3 m, with larger discrepancies at the edges of the islands, such as around 20.77° N, 116.8° E (Dongsha Group; Fig. 11b2) and 8.14° N, 113.3° E (Yuniao Reef; Fig. 11e2). These discrepancies can be attributed to two main factors. First, the quality of the ICESat-2 data tends to degrade near boundaries, owing to the complex boundary topography and environmental conditions, thus affecting the accuracy of the depth measurements. Second, there is a significant edge effect in the SDB modeling: as the number of ICESat-2 data points decreases, the constraints on the linear regression model are reduced and the estimation accuracy declines.

The SDB training and validation results are presented in Fig. 11 in columns 3 and 4, respectively. Based on the training results, for the six representative islands, the RMSEs are from 0.54 to 1.20 m and the regression slopes are from 0.90 to 1.05. This reveals high consistency and robust performance using the training dataset. The high R^2 values demonstrate a strong correlation between the model predictions and the actual observations, while the low RMSE confirms the accuracy of the model in predicting water depths in shallow areas.

For the six islands, the validation results reveal RMSEs of 0.46–1.24 m and regression slopes of 0.85–1.13. As with the training results, the validation results reveal a strong correlation between the model predictions and the actual observations. The regression slopes (which are close to unity) indicate that the model performs well not only on training data but also on unseen data, reflecting its robust generalization capability. Along with the results illustrated in Figs. 9 and 10, this shows that the model maintains a consistently high performance throughout both the training and validation phases, thus highlighting its stability and reliability.

We next analyzed the SDB validation results for all 128 islands and reefs against the ICESat-2 data. Over 90 % of the SDB results exhibit a RMSE consistently below 5 % of the maximum depth. The lower modeling accuracy for specific islands and reefs (such as the Daxian Reef, Fig. 8c, and the Banlu Reef, Fig. 8d) can be attributed to the scarcity and uneven distribution of effective water depth data in the ICESat-2 dataset and the high level of noise in the images. These results demonstrate that the SDB model effectively captured

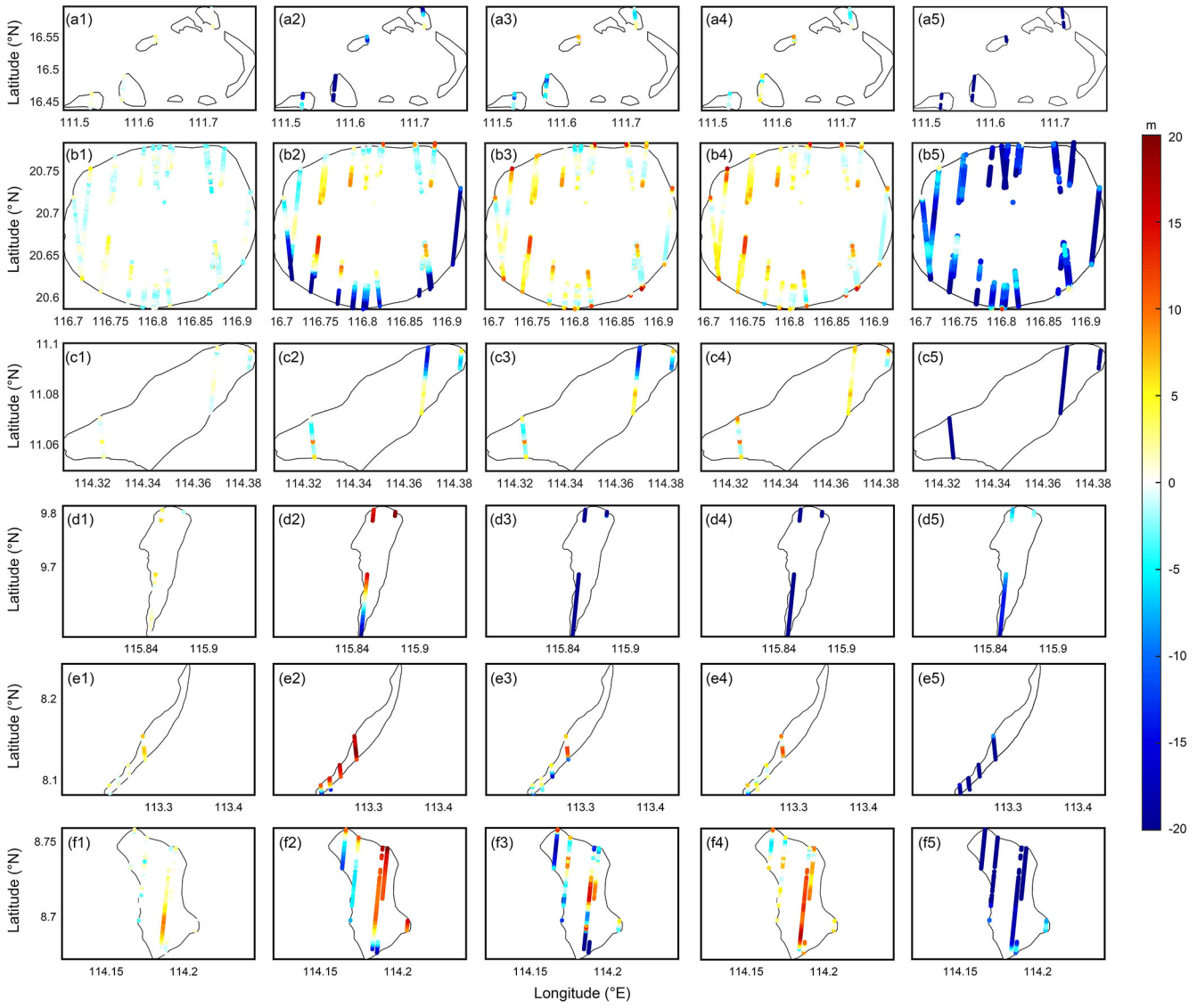

Figure 13. Validation of HHU24SWDSCS (first column, **a1–f1**), DTU18BAT (second column, **a2–f2**), topo_27.1 (third column, **a3–f3**), SRTM15 + V2.6 (fourth column, **a4–f4**), and GEBCO_2024 (fifth column, **a5–f5**) against independent ICESat-2 water depth data. The six rows represent the results in the Yongle islands, Dongsha islands, Meijiu islands, Renai islands, Yuniao islands, and Nanhua islands, respectively.

the fine-scale bathymetric features of shallow-water areas. Incorporating the control data (the ICESat-2 depth data) effectively constrained and enhanced the absolute accuracy of the SDB model. By leveraging the complementary advantages of multi-source remote-sensing data, the precision of the SDB results is ensured.

Using airborne bathymetry data (SIOFM) for the shallow waters near the Lingyang Reef, the reef's bathymetry was validated. The latest global bathymetry models, including DTU18BAT (DTU Space), topo_27.1 and SRTM15 + V2.6 (SIO), and GEBCO_2024 (GEBCO Bathymetric Compilation Group), were introduced for validation and analysis. We used nearest-neighbor interpolation to interpolate the bathymetry models to the airborne lidar bathymetry points. Based on the validation results (Fig. 12), the SDB model achieves notably better estimates than the other models. As shown in Fig. 12a, the differences between the SDB-derived bathymetry and the validation data are mostly within ±3 m, whereas the discrepancies exceed 10 m with respect to the other models. Given that the water depth ranges from 0 to 10 m in the shallow-water areas of the Lingyang Reef, this indicates that the existing bathymetry models exhibit relatively poor accuracy and low data reliability in these regions. The RMSE is 1.01 m for the SDB model, as opposed to 61.03 m for DTU18BAT, 25.03 m for topo_27.1, 4.3 m for SRTM15 + V2.6, and 32.38 m for GEBCO_2024 (Table 3).

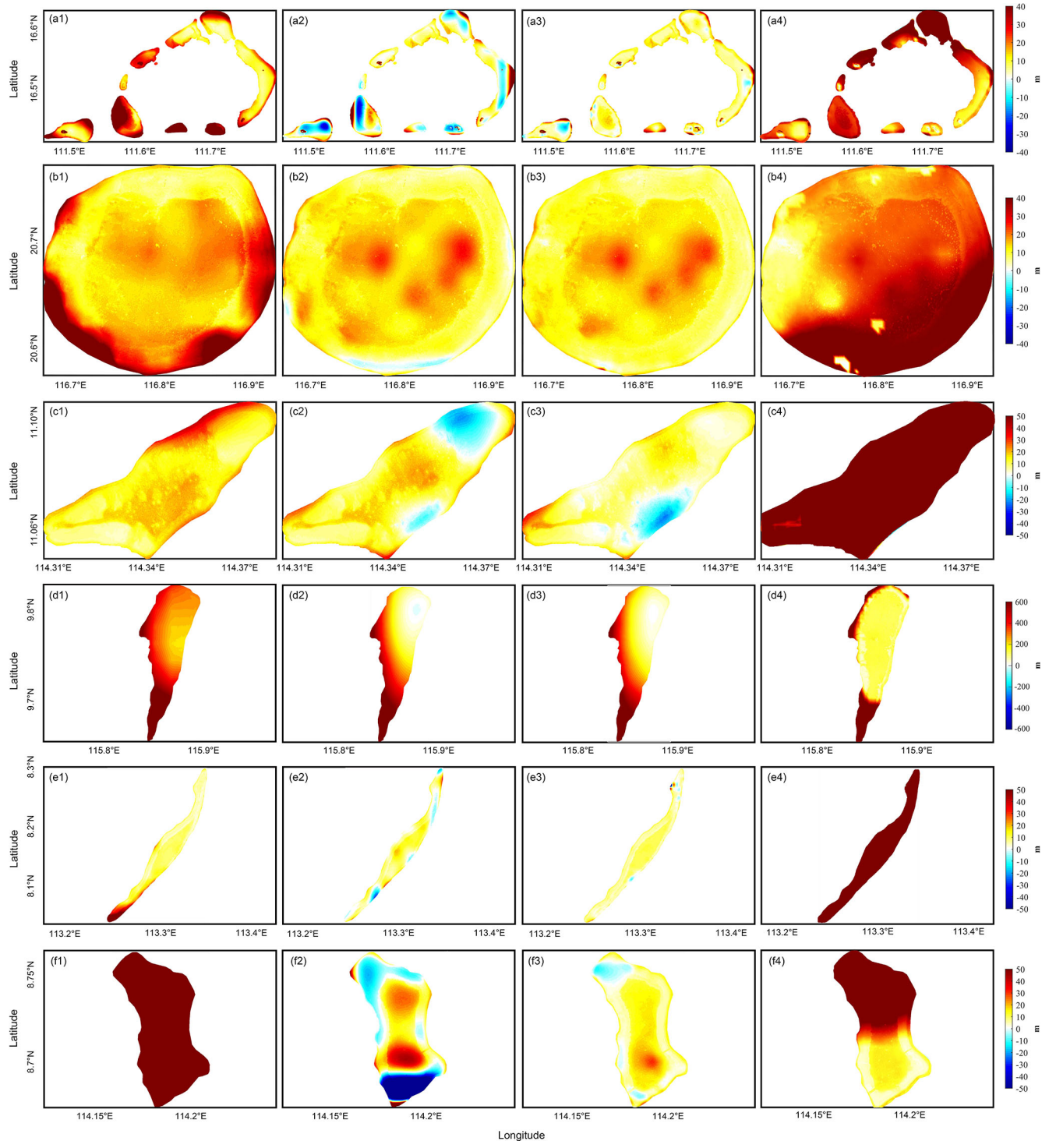

Figure 14. The comparison of the representative reefs between the SDB results and DTU18BAT (first column), topo_27.1 (second column), SRTM15 + V2.6 (third column), and GEBOCO_2023 (fourth column), respectively.

Table 4. Statistics of the misfits between the different bathymetry models and the ICESat-2 validation data over the six representative reefs (m).

Research area	Models	Maximum	Minimum	Mean	RMSE
Yongle Group	SDB	3.49	−1.31	0.65	0.77
	DTU18BAT	2.26	−91.81	−48.09	56.93
	topo_27.1	7.78	−12.85	−5.26	7.12
	SRTM15 + V2.6	8.69	−5.39	−0.62	2.43
	GEBCO_2024	−9.5	−137.84	−46.07	52.35
Dongsha Group	SDB	8.26	−7.95	−0.50	1.25
	DTU18BAT	13.00	−92.41	−5.64	12.66
	topo_27.1	16.48	−5.86	0.07	2.52
	SRTM15 + V2.6	16.54	−7.10	0.80	2.68
	GEBCO_2024	0.11	−103.94	−21.81	28.11
Meijiu Reef	SDB	5.05	−3.46	−0.12	1.02
	DTU18BAT	9.39	−18.80	−4.28	7.43
	topo_27.1	9.25	−21.54	−4.65	8.64
	SRTM15 + V2.6	10.28	−2.82	1.18	2.89
	GEBCO_2024	−56.65	−432.38	−223.53	245.51
Renai Reef	SDB	6.52	−3.23	0.38	1.16
	DTU18BAT	−271.25	−1.129.47	−682.67	727.91
	topo_27.1	−8.38	−901.05	−548.55	599.55
	SRTM15 + V2.6	−42.11	−888.34	−526.29	573.64
	GEBCO_2024	−2.11	−203.03	−60.19	89.47
Yuniao Reef	SDB	6.98	−2.68	0.39	1.35
	DTU18BAT	9.85	−103.13	−22.44	36.34
	topo_27.1	12.14	−20.22	−2.38	6.88
	SRTM15 + V2.6	11.42	−14.52	−1.09	5.25
	GEBCO_2024	−136.75	−231.43	−175.62	177.45
Nanhua Reef	SDB	9.47	−4.1	0.33	1.54
	DTU18BAT	−45.36	−212.57	−116.03	123.41
	topo_27.1	20.89	−141.41	−12.95	32.25
	SRTM15 + V2.6	17.26	−6.02	1.86	5.57
	GEBCO_2024	−1.77	−252.42	−118.55	136.19

These validation results show that the SDB model can provide shallow-water bathymetry with ∼ 1 m accuracy, consistent with the independent ICESat-2-based validation results (Fig. 10). More importantly, the SDB model significantly outperforms other existing models for shallow-water areas.

4.2 Discussion

Given that most marine-related production and economic activities are concentrated in shallow-water areas, accurate shallow-water bathymetry has become essential in such activities. Therefore, it is necessary to evaluate the accuracy of the existing bathymetry models further for coastal shallow-water areas. Validation results for the existing bathymetry models for representative reef areas using ICESat-2 data are shown in Fig. 13; each column represents the validation results for one model (SDB, DTU18BAT, topo_27.1, SRTM15 + V2.6, and GEBCO_2024), each row, and the performance for a specific reef. For all six reefs, the SDB-derived bathymetry results differ from the validation data by < 5 m, whereas for the other models these differences exceed 20 m. Specifically, as shown in Table 4, the SDB validation RMSEs are 0.77, 1.25, 1.02, 1.16, 1.35, and 1.54 m, respectively, whereas for DTU18BAT, topo_27.1, SRTM15 + V2.6, and GEBCO_2024 the RMSEs exceed 2 m, even reaching tens of meters (Table 4). Given that the water depth in coastal shallow-water areas is generally < 30 m, most of the existing bathymetry models exhibit high uncertainties and low data usability. In contrast, the SDB model achieves relatively robust meter-level accuracy in these regions, demonstrating its superiority in shallow-water bathymetry retrieval. Notably, the existing bathymetry models and the validation data differ significantly for the Renai Reef area, with a maximum difference exceeding 700 m, while the difference between the SDB results and the validation data for this reef is reduced to the meter level. This discrepancy may be because the existing

Table 5. Statistics of the misfits between the different bathymetry models and the SDB results over the six representative reefs (m).

Research area	Models	Maximum	Minimum	Mean	RMSE
Yongle Group	DTU18BAT	137.99	1.08	22.42	30.26
	topo_27.1	111.27	−35.58	2.14	14.08
	SRTM15 + V2.6	89.47	−16.86	5.73	8.52
	GEBCO_2024	179.45	−7.33	40.74	50.91
Dongsha Group	DTU18BAT	126.39	1.06	17.64	22.34
	topo_27.1	27.67	−7.89	10.60	11.75
	SRTM15 + V2.6	32.65	−4.03	10.35	11.26
	GEBCO_2024	103.97	−2.58	31.86	36.14
Meijiu Reef	DTU18BAT	43.15	2.85	14.91	16.12
	topo_27.1	39.08	−23.78	8.28	12.58
	SRTM15 + V2.6	36.16	−25.36	5.91	9.48
	GEBCO_2024	498.06	32.92	278.12	293.10
Renai Reef	DTU18BAT	1172.07	189.36	398.25	447.78
	topo_27.1	946.65	−10.01	273.63	355.63
	SRTM15 + V2.6	935.88	2.44	255.41	332.35
	GEBCO_2024	376.35	1.11	27.69	58.33
Yuniao Reef	DTU18BAT	113.06	1.57	11.09	17.66
	topo_27.1	35.70	−29.71	5.60	8.79
	SRTM15 + V2.6	41.13	−117.54	5.95	7.35
	GEBCO_2024	441.01	−74.58	218.29	228.07
Nanhua Reef	DTU18BAT	306.60	59.61	130.26	135.83
	topo_27.1	176.34	−141.35	−2.99	36.47
	SRTM15 + V2.6	31.42	−13.06	8.67	11.27
	GEBCO_2024	268.85	1.00	67.96	95.54

models rely primarily on satellite-altimetry-derived gravity anomalies for water depth data due to the scarcity of in situ measurements. However, the poor quality of altimetry data near the coast leads to significant errors in the bathymetry models. Based on the validation results presented in Figs. 12 and 13, the SDB bathymetry model achieves high accuracy and robustness in coastal shallow-water areas.

Furthermore, benefiting from the rich spatial information of the SDB model, the spatial detail and accuracy of the existing bathymetry models are analyzed. The differences between the SDB results and those of the DTU18BAT, topo_27.1, SRTM15 + V2.6, and GEBCO_2024 models were calculated for the representative reefs (Fig. 14). This revealed relatively large differences, with maximum discrepancies exceeding 50 m. Statistically, the RMSEs of the differences between the DTU18BAT, topo_27.1, SRTM15 + V2.6, and GEBCO_2024 models against the SDB results reach tens of meters across the six typical island regions, particularly for the Renai Reef area, for which the RMSE exceeds 100 m (Table 5).

These results show that the existing bathymetry models are significantly deficient in spatial resolution, modeling accuracy, and detailed signal depiction for coastal shallow-water areas, making it difficult to meet the current demands of navigation, nearshore economic activities, port construction, and other production activities. The SDB model, which achieves 10 m spatial resolution, meter-level modeling accuracy, detailed bathymetry signals, efficiency, and low cost, therefore constitutes an improvement for coastal shallow-water areas and provides fundamental data support for research in oceanography, geodesy, and other disciplines.

Nonetheless, the sources of error in the SDB results cannot be ignored. First, their accuracy is substantially influenced by water conditions, including turbidity, water type, and water color, which directly affect the underwater light penetration and reflectance measurements of remote-sensing images (Caballero and Stumpf, 2020, 2023). Additionally, although the Sentinel-2 images used in this study have undergone correction for atmospheric effects, residual errors from atmospheric effects, image noise, and the influence of Sun glint may still reduce the quality of the SDB results (Warren et al., 2019). The quality of the ICESat-2 data is another key factor in SDB modeling, as their signal-to-noise ratio and limited deep-water penetration capabilities may lead to insufficient underwater topographic information retrieval. Regarding the selection of the SDB estimation methods, the empirical methods rely on a priori depth data to establish the relationship between reflectance and water depth. However,

this relationship becomes nonlinear in deeper waters, making SDB estimates unreliable in deep-water areas (Ashphaq et al., 2021; Wu et al., 2024b). Furthermore, the impact of changes over time on underwater topography should not be overlooked, as sedimentation, erosion, ocean currents, and human activities can all alter shallow-water bathymetry over time (Caballero and Stumpf, 2021; Niroumand-Jadidi et al., 2020).

5 Data availability

The HHU24SWDSCS model is openly accessible at https://doi.org/10.5281/zenodo.13852568 (Wu et al., 2024a). The dataset file (HHU24SWDSCS.nc) includes geospatial information (latitude and longitude), shallow-water depth, and the distribution of the reefs. The Mapper5000 airborne lidar bathymetric dataset is provided by the Shanghai Institute of Optics and Fine Mechanics, Chinese Academy of Sciences. DTU18BAT provided by DTU Space is available at https://ftp.space.dtu.dk/pub/DTU18/1_MIN/ (Andersen, 2018). SRTM15+V2.6 and topo_27.1 provided by the Scripps Institution of Oceanography are freely available at https://topex.ucsd.edu/pub/global_topo_1min/ (Sandwell et al., 2025). GEBCO_2024 provided by the GEBCO group is available at https://doi.org/10.5285/1c44ce99-0a0d-5f4f-e063-7086abc0ea0f (GEBCO Compilation Group, 2024). The authors would also like to thank NASA's National Snow and Ice Data Center for providing the ICESat-2 data (https://doi.org/10.5067/ATLAS/ATL03.006, Neumann et al., 2023) and the Sentinel Scientific Data Hub of the European Space Agency for providing the Sentinel-2 data (https://doi.org/10.5270/S2_-znk9xsj, Copernicus Sentinel-2, 2021).

6 Conclusions

Accurate shallow-water bathymetric data are essential for maritime safety, resource exploration, ecological conservation, and oceanic economic development. To address these requirements, we developed the HHU24SWDSCS model using ICESat-2 data and Sentinel-2 high-resolution multispectral imagery to construct detailed bathymetric maps over 120 islands and reefs in the SCS region. A comprehensive framework was developed to integrate the ICESat-2 data and Sentinel-2 imagery for shallow-water bathymetry modeling.

The accuracy and consistency of the SDB model were evaluated using independent ICESat-2 bathymetry data, which demonstrated robust performance with an RMSE of 0.82 m, underscoring their reliability across the SCS region. Further validation in the Lingyang Reef using the airborne lidar bathymetry data revealed that the SDB model achieved superior accuracy (1.01 m) compared to traditional models. Comprehensive validation of the latest bathymetry models (i.e., DTU18BAT, topo27.1, SRTM15 + V2.6, and GEBCO_2024) was conducted against the ICESat-2, airborne lidar, and SDB data for the shallow-water regions of the representative reefs. This assessment highlighted significant uncertainties, low spatial resolution, and a lack of detail in these existing models in coastal regions and shallow waters. Overall, the SDB model represents a significant advancement in shallow-water bathymetry, offering enhanced accuracy, spatial resolution, and coverage and making it a viable alternative to existing bathymetry models and a powerful tool for marine applications, including coastal construction, ecological conservation, petroleum exploration, and scientific research.

In future, we will aim to leverage ICESat-2 and Sentinel-2 data for feature extraction and labeling, utilizing deep-learning techniques to construct detailed bathymetric maps of global shallow-water regions. Critical environmental factors such as water quality, water color, seafloor characteristics, and illumination conditions should be considered during model training to enhance generalization capabilities across diverse marine environments. By integrating multiple data sources, including ICESat-2 water depth data, SDB data, satellite altimetry data, and multibeam sonar sounding, we aim to develop a high-precision, seamless bathymetry model for both shallow and deep waters. Furthermore, the developed SDB technology holds significant potential for coastal and estuarine applications, particularly in monitoring sediment dynamics and investigating temporal variations in intertidal regions.

Appendix A

Table A1. Information on the research areas and distribution of the islands.

Research areas	Island group	Island name	Latitude (° N)	Longitude (° E)	Research areas	Island group	Sea	Latitude (° N)	Longitude (° E)
Area 1	Xuande Group	Yongxing	16.83	112.33	Area 3	Jiuzhang Group	Jinghong	9.88	114.32
		Shi	16.85	112.35			Nanmen Reef	9.90	114.40
		Xi Sand	16.97	112.20			Ximen Reef	9.90	114.47
		Zhaoshu	16.97	112.27			Dongmen Reef	9.92	114.50
		Bei	16.97	112.30			Anle Reef	9.93	114.52
		Zhong	16.95	112.32			Changxian Reef	9.93	114.55
		Nan	16.93	112.33			Zhuquan Reef	9.95	114.57
		Bei Reef	16.93	112.33			Niue Reef	9.97	114.62
		Zhong Reef	16.93	112.33			Ranqing Reef	9.88	114.60
		Nan Reef	16.92	112.33			Ranqing Sand	9.90	114.57
		Dongxin Reef	16.92	112.35			Longxia Reef	9.88	114.53
		Xixin Reef	16.92	112.35			Bianshen Reef	9.87	114.52
	Dongdao Atoll	Dong	16.67	112.73			Zhangxi Reef	9.83	114.47
		Gaojian Reef	16.57	112.63			Quyuan Reef	9.80	114.40
		Beibian Reef	16.53	112.55			Qiong Reef	9.75	114.35
		Zhanhan Band	16.42	112.62			Chigua Reef	9.70	114.28
	Langhua Reef		16.05	112.55			Guihan Reef	9.77	114.25
	Yongle Group	Ganquan	16.50	111.58			Hua Reef	9.85	114.27
		Shanhu	16.53	111.60			Jiyang Reef	9.87	114.28
		Jinyin	16.43	111.50		Huoai Reef		10.88	114.93
		Zhenhang	16.45	111.70		Xiyue		11.07	115.02
		Guangjin	16.45	111.70		Daxian Reef		10.07	113.87
		Jinqing	16.45	111.73		Sanjiao Reef		10.17	115.32
		Lingyang Reef	16.45	111.58	Area 4	Antang Reef		10.88	116.43
		Quanfu	16.57	111.67		Donghua Reef		10.55	116.93
		Yagong	16.57	111.68		Wufang Group	Wufang Reef	10.48	115.75
		Yin Reef	16.58	111.70			Wufangnan Reef	10.45	115.77
		Yinyuzi	16.58	111.70			Wufangwei Reef	10.47	115.72
		Xianshe Reef	16.55	111.72			Wufangxi Reef	10.50	115.70
		Kuangzi Sand	16.45	111.63			Wufangbei Reef	10.53	115.72
		Shi Reef	16.55	111.75			Wufangtou Reef	10.53	115.78
	Huaguang Reef		16.20	111.67		Banlu Reef		10.13	116.13
	Yuzhuo Reef		16.33	112.02		Yongshi Bank		11.08	117.47
	Panshi Reef		16.05	111.77		Xiane Reef		9.35	115.43
	Bei Reef		17.08	111.50		Xinyi Reef		9.33	115.95
	Zhongjian Reef		15.78	111.20		Haikou Shoal		9.18	116.45
Area 2	Dongsha Group	Dongsha	20.72	116.70		Banyue Shoal		8.87	116.27
		Dongsha Reef	20.67	116.90		Yenai Reef		9.72	115.88
Area 3	Shuangzi Reef	Gongshi Reef	11.47	114.40		Xianbin Reef		9.73	116.57
		Beizi	11.45	114.35		Niuche Reef		9.60	116.17
		Beiwai Reef	11.45	114.35	Area 5	Yongshu Reef		9.58	112.97
		Nanzi	11.43	114.33		Yinqing Group	Xi Reef	8.87	112.23
		Nailuo Reef	11.38	114.30			Dong Reef	8.83	112.58
		Dongnan Shoal	11.40	114.37			Huayang Reef	8.88	112.85
		Dongbei Shoal	11.43	114.40			Yuniao Reef	8.27	113.37
		Beizi Shoal	11.43	114.38		Riji Reef		8.67	111.67
	Zhongye Group	Zhongye	11.05	114.28	Area 6	Wunie Reef		8.87	114.65
		Tiezhi Reef	11.08	114.38		Nanhua Reef		8.75	114.18
		Meijiu Reef	11.05	114.32		Liumen Reef		8.83	113.98
		Tiexian Reef	11.07	114.23		Bisheng Reef		8.97	113.67
	Daoming Group	Shuanghuang Reef	10.70	114.32		Erjiao Reef		8.20	114.70
		Nanyue	10.67	114.42		Yuya Group	Langkou Reef	8.13	114.55
		Yangxin Cay	10.70	114.52			Xiantou Reef	8.13	114.80
		Kugui Reef	10.77	114.58			Guangxingzi Reef	7.62	113.93
	Zhenghe Group	Taiping	10.38	114.37		Siling Reef		8.37	115.23
		Zhong Bank	10.37	114.38		Boji Reef		8.10	114.13
		Zhongzhou Reef	10.38	114.42		Guangxing Reef		7.63	113.80
		Chunqian Sand	10.38	114.47		Nanhai Reef		7.98	113.88
		Bolan Reef	10.42	114.58		Danwan Reef		7.37	113.83
		Anda Reef	10.35	114.70		Huanglu Reef		6.95	113.58
		Hongxiu	10.18	114.37		Nantong Reef		6.33	113.23
		Nanxun Reef	10.20	114.23	Area 7	Nanan Reef		5.53	112.58
	Yongdeng Shoal		11.40	114.67		Nanping Reef		5.37	112.63
	Lesi Shoal		11.33	114.62		Haining Reef		4.95	112.62

Author contributions. YW and HS presented the algorithm and obtained the experimental results. YW, HS, and DJ prepared the paper and figures with contributions from all the co-authors. YW, HS, DJ, OA, XH, and ZL polished the entire manuscript. YL, SC, XS, YS, SD, and YC downloaded the ICESat-2 and Sentinel-2 data as well as the other products in this work. All the authors checked and made relevant comments on this work.

Competing interests. The contact author has declared that none of the authors has any competing interests.

Disclaimer. Publisher's note: Copernicus Publications remains neutral with regard to jurisdictional claims made in the text, published maps, institutional affiliations, or any other geographical representation in this paper. While Copernicus Publications makes every effort to include appropriate place names, the final responsibility lies with the authors.

Financial support. This work was supported by the National Natural Science Foundation of China (grant no. 42374099), the Jiangsu Funding Program for Excellent Postdoctoral Talent under grant no. 2024ZB632, the Fundamental Research Funds for the Central Universities (grant no. B240201097), the State Scholarship Fund of the Chinese Scholarship Council (grant nos. 201306270014 and 202006710169), the Project of the China Railway Corporation (grant nos. 2021-key-14 and 2021-major-08), and the Joint Planning of Technology and Water Conservancy of Jiangxi Province (grant no. 2022KSG01009).

Review statement. This paper was edited by Sebastiano Piccolroaz and reviewed by three anonymous referees.

References

Abdalati, W., Zwally, H. J., Bindschadler, R., Csatho, B., Farrell, S. L., Fricker, H. A., Harding, D., Kwok, R., Lefsky, M., and Markus, T.: The ICESat-2 laser altimetry mission, P. IEEE, 98, 735–751, https://doi.org/10.1109/JPROC.2009.2034765, 2010.

Albright, A. and Glennie, C.: Nearshore bathymetry from fusion of Sentinel-2 and ICESat-2 observations, IEEE Geosci. Remote S., 18, 900–904, https://doi.org/10.1109/LGRS.2020.2987778, 2020.

An, D., Guo, J., Chang, X., Wang, Z., Jia, Y., Liu, X., Bondur, V., and Sun, H.: High-precision $1' \times 1'$ bathymetric model of Philippine Sea inversed from marine gravity anomalies, Geosci. Model Dev., 17, 2039–2052, https://doi.org/10.5194/gmd-17-2039-2024, 2024.

Andersen, O. B.: DTU18BAT_1min.bat, DTU [data set], https://ftp.space.dtu.dk/pub/DTU18/1_MIN/ (last access: 28 May 2025), 2018.

Andersen, O. B. and Knudsen, P.: The DNSC08BAT bathymetry developed from satellite altimetry, in: EGU-2008 Meeting, Vienna, Austria, https://www.space.dtu.dk/english/-/media/institutter/space/newdesign_2023/forskning/scientific-data-and-models/dnsc08bat.pdf (last access: 18 September 2024), 2008.

Ashphaq, M., Srivastava, P. K., and Mitra, D.: Review of near-shore satellite derived bathymetry: classification and account of five decades of coastal bathymetry research, J. Ocean. Eng. Sci., 6, 340–359, https://doi.org/10.1016/j.joes.2021.02.006, 2021.

Babonneau, N., Delacourt, C., Cancouët, R., Sisavath, E., Bachèlery, P., Mazuel, A., Jorry, S. J., Deschamps, A., Ammann, J., and Villeneuve, N.: Direct sediment transfer from land to deep-sea: insights into shallow multibeam bathymetry at La Réunion island, Mar. Geol., 346, 47–57, https://doi.org/10.1016/j.margeo.2013.08.006, 2013.

Benesty, J., Chen, J., Huang, Y., and Cohen, I.: Pearson correlation coefficient, in: Noise Reduction in Speech Processing, vol. 2, Springer Berlin Heidelberg, Berlin, Heidelberg, 1–4, https://doi.org/10.1007/978-3-642-00296-0_5, 2009.

Bergstad, O. A., Høines, Å. S., Sarralde, R., Campanis, G., Gil, M., Ramil, F., Maletzky, E., Mostarda, E., Singh, L., and António, M.: Bathymetry, substrate and fishing areas of southeast atlantic high-seas seamounts, Afr. J. Mar. Sci., 41, 11–28, https://doi.org/10.2989/1814232X.2019.1569160, 2019.

Caballero, I. and Stumpf, R.: Towards Routine Mapping of Shallow Bathymetry in Environments with Variable Turbidity: Contribution of Sentinel-2A/B Satellites Mission, Remote Sens., 12, 451, https://doi.org/10.3390/rs12030451, 2020.

Caballero, I. and Stumpf, R. P.: On the use of sentinel-2 satellites and lidar surveys for the change detection of shallow bathymetry: the case study of north carolina inlets, Coast. Eng., 169, 103936, https://doi.org/10.1016/j.coastaleng.2021.103936, 2021.

Caballero, I. and Stumpf, R. P.: Confronting turbidity, the major challenge for satellite-derived coastal bathymetry, Sci. Total Environ., 870, 161898, https://doi.org/10.1016/j.scitotenv.2023.161898, 2023.

Cesbron, G., Melet, A., Almar, R., Lifermann, A., Tullot, D., and Crosnier, L.: Pan-european satellite-derived coastal bathymetry – review, user needs and future services, Front. Mar. Sci., 8, 740830, https://doi.org/10.3389/fmars.2021.740830, 2021.

Copernicus Sentinel-2: MSI Level-2A BOA Reflectance Product. Collection 1, European Space Agency [data set], https://doi.org/10.5270/S2_-znk9xsj, 2021.

Costa, B., Battista, T., and Pittman, S.: Comparative evaluation of airborne LiDAR and ship-based multibeam SoNAR bathymetry and intensity for mapping coral reef ecosystems, Remote Sens. Environ., 113, 1082–1100, https://doi.org/10.1016/j.rse.2009.01.015, 2009.

Drusch, M., Del Bello, U., Carlier, S., Colin, O., Fernandez, V., Gascon, F., Hoersch, B., Isola, C., Laberinti, P., and Martimort, P.: Sentinel-2: ESA's optical high-resolution mission for GMES operational services, Remote Sens. Environ., 120, 25–36, https://doi.org/10.1016/j.rse.2011.11.026, 2012.

Ernstsen, V. B., Noormets, R., Hebbeln, D., Bartholomä, A., and Flemming, B. W.: Precision of high-resolution multibeam echo sounding coupled with high-accuracy positioning in a shallow water coastal environment, Geo-Mar. Lett., 26, 141–149, https://doi.org/10.1007/s00367-006-0025-3, 2006.

Ferreira, I. O., Andrade, L. C. de, Teixeira, V. G., and Santos, F. C. M.: State of art of bathymetric surveys, Bol. Ciênc. Geod., 28, e2022002, https://doi.org/10.1590/s1982-21702022000100002, 2022.

Folorunso, A. F. and Li, Y.: Seafloor bathymetry in deep and shallow water marine CSEM responses of nigerian niger delta oil field: effects and corrections, J. Appl. Geophys., 123, 194–210, https://doi.org/10.1016/j.jappgeo.2015.10.014, 2015.

Gao, B.-C.: NDWI – a normalized difference water index for remote sensing of vegetation liquid water from space, Remote Sens. Environ., 58, 257–266, https://doi.org/10.1016/S0034-4257(96)00067-3, 1996.

Gatti, A. and Bertolini, A.: Sentinel-2 products specification document, Rapp. tech., 4–7, https://sentinel.esa.int/documents/247904/349490/S2_MSI_Product_Specification.pdf (last access: 18 September 2024), 2015.

Ge, B., Guo, J., Kong, Q., Zhu, C., Huang, L., Sun, H., and Liu, X.: Seafloor topography inversion from multi-source marine gravity data using multi-channel convolutional neural network, Eng. Appl. Artif. Intel., 139, 109567, https://doi.org/10.1016/j.engappai.2024.109567, 2025.

GEBCO Compilation Group: GEBCO 2024 Grid, National Oceanography Center [data set], https://doi.org/10.5285/1c44ce99-0a0d-5f4f-e063-7086abc0ea0f, 2024.

Goodman, J. A., Lay, M., Ramirez, L., Ustin, S. L., and Haverkamp, P. J.: Confidence levels, sensitivity, and the role of bathymetry in coral reef remote sensing, Remote Sens., 12, 496, https://doi.org/10.3390/rs12030496, 2020.

Guenther, G. C.: Airborne lidar bathymetry, Digital elevation model technologies and applications: the DEM users manual, American Society for Photogrammetry & Remote Sensing, 2, 253–320, https://coast.noaa.gov/data/docs/geotools/2017/presentations/Maune.pdf (last access: 18 September 2024), 2007.

Guo, X., Jin, X., and Jin, S.: Shallow water bathymetry mapping from ICESat-2 and Sentinel-2 based on BP neural network model, Water, 14, 3862, https://doi.org/10.3390/w14233862, 2022.

Hodúl, M., Bird, S., Knudby, A., and Chénier, R.: Satellite derived photogrammetric bathymetry, ISPRS J. Photogramm., 142, 268–277, https://doi.org/10.1016/j.isprsjprs.2018.06.015, 2018.

Hsu, H.-J., Huang, C.-Y., Jasinski, M., Li, Y., Gao, H., Yamanokuchi, T., Wang, C.-G., Chang, T.-M., Ren, H., Kuo, C.-Y., and Tseng, K.-H.: A semi-empirical scheme for bathymetric mapping in shallow water by ICESat-2 and sentinel-2: a case study in the south China sea, ISPRS J. Photogramm., 178, 1–19, https://doi.org/10.1016/j.isprsjprs.2021.05.012, 2021.

Huang, Q., Wang, W., Li, Y., and Li, C.: Current characteristics of the South China Sea, in: Oceanology of China Seas, edited by: Di, Z., Yuan-Bo, L., and Cheng-Kui, Z., Springer Netherlands, Dordrecht, 39–47, https://doi.org/10.1007/978-94-011-0862-1_5, 1994.

Hwang, C.: A bathymetric model for the south China sea from satellite altimetry and depth data, Mar. Geod., 22, 37–51, https://doi.org/10.1080/014904199273597, 1999.

Jia, D., Li, Y., He, X., Yang, Z., Wu, Y., Wu, T., and Xu, N.: Methods to improve the accuracy and robustness of satellite-derived bathymetry through processing of optically deep waters, Remote Sens., 15, 5406, https://doi.org/10.3390/rs15225406, 2023.

Kirby, K., Ferguson, S., Rennie, C. D., Cousineau, J., and Nistor, I.: Identification of the best method for detecting surface water in sentinel-2 multispectral satellite imagery, Remote Sens. Appl. Soc. Environ., 36, 101367, https://doi.org/10.1016/j.rsase.2024.101367, 2024.

Li, J., Tao, B., He, Y., Li, Y., Huang, H., Mao, Z., and Yu, J.: Range difference between shallow and deep channels of airborne bathymetry LiDAR with segmented field-of-view receivers, IEEE T. Geosci. Remote, 60, 1–16, https://doi.org/10.1109/TGRS.2022.3172351, 2022.

Lyzenga, D. R., Malinas, N. P., and Tanis, F. J.: Multispectral bathymetry using a simple physically based algorithm, IEEE T. Geosci. Remote, 44, 2251–2259, https://doi.org/10.1109/TGRS.2006.872909, 2006.

Ma, Y., Xu, N., Liu, Z., Yang, B., Yang, F., Wang, X. H., and Li, S.: Satellite-derived bathymetry using the ICESat-2 lidar and sentinel-2 imagery datasets, Remote Sens. Environ., 250, 112047, https://doi.org/10.1016/j.rse.2020.112047, 2020.

Markus, T., Neumann, T., Martino, A., Abdalati, W., Brunt, K., Csatho, B., Farrell, S., Fricker, H., Gardner, A., and Harding, D.: The ice, cloud, and land elevation satellite-2 (ICESat-2): science requirements, concept, and implementation, Remote Sens. Environ., 190, 260–273, https://doi.org/10.1016/j.rse.2016.12.029, 2017.

Martino, A. J., Neumann, T. A., Kurtz, N. T., and McLennan, D.: ICESat-2 mission overview and early performance, in: Sensors, systems, and next-generation satellites XXIII, 68–77, https://doi.org/10.1117/12.2534938, 2019.

Mavraeidopoulos, A. K., Pallikaris, A., and Oikonomou, E.: Satellite derived bathymetry (SDB) and safety of navigation, Int. Hydrogr. Rev., 30, https://journals.lib.unb.ca/index.php/ihr/article/view/26290 (last access: 18 September 2024), 2017.

Misra, A. and Ramakrishnan, B.: Assessment of coastal geomorphological changes using multi-temporal satellite-derived bathymetry, Cont. Shelf Res., 207, 104213, https://doi.org/10.1016/j.csr.2020.104213, 2020.

Neumann, T., Brenner, A., Hancock, D., Robbins, J., Saba, J., Harbeck, K., Gibbons, A., Lee, J., Luthcke, S., and Rebold, T.: ATLAS/ICESat-2 L2A global geolocated photon data, version 3, Boulder, Colorado USA, NASA National Snow and Ice Data Center Distributed Active Archive Center [data set], https://doi.org/10.5067/ATLAS/ATL03.006, 2021.

Neumann, T. A., Brenner, A., Hancock, D., Robbins, J., Gibbons, A., Lee, J., Harbeck, K., Saba, J., Luthcke, S. B., and Rebold, T.: ATLAS/ICESat-2 L2A Global Geolocated Photon Data (ATL03, Version 6), NASA National Snow and Ice Data Center Distributed Active Archive Center [data set], https://doi.org/10.5067/ATLAS/ATL03.006, 2023.

Niroumand-Jadidi, M., Bovolo, F., and Bruzzone, L.: SMART-SDB: sample-specific multiple band ratio technique for satellite-derived bathymetry, Remote Sens. Environ., 251, 112091, https://doi.org/10.1016/j.rse.2020.112091, 2020.

Parker, B.: The integration of bathymetry, topography and shoreline and the vertical datum transformations behind it, Int. Hydrogr. Rev., 3, https://journals.lib.unb.ca/index.php/ihr/article/view/18616 (last access: 18 September 2024), 2002.

Pitcher, T. J., Watson, R., Haggan, N., Guénette, S., Kennish, R., Sumaila, U. R., Cook, D., Wilson, K., and Leung, A.: Marine reserves and the restoration of fisheries and marine ecosystems in the south China sea, Bull. Mar. Sci., 66, 543–566, https://www.researchgate.net/publication/233703204_Marine_Reserves_and_the_Restoration_of_Fisheries_and_Marine_Ecosystems_in_the_South_China_Sea (last access: 18 September 2024), 2000.

Ruan, X., Cheng, L., Chu, S., Yan, Z., Zhou, X., Duan, Z., and Li, M.: A new digital bathymetric model of the south China sea based on the subregional fusion of seven global seafloor topography products, Geomorphology, 370, 107403, https://doi.org/10.1016/j.geomorph.2020.107403, 2020.

Sandwell, D. T., Müller, R. D., Smith, W. H., Garcia, E., and Francis, R.: New global marine gravity model from CryoSat-2 and jason-1 reveals buried tectonic structure, Science, 346, 65–67, https://doi.org/10.1126/science.1258213, 2014.

Sandwell, D. T., Smith, W. H., and Becker, J. J.: SRTM15+V2.6 and topo_27.1, UCSD [data set], https://topex.ucsd.edu/pub/global_topo_1min/, (last access: 28 May 2025), 2025.

Schneider von Deimling, J. and Weinrebe, W.: Beyond bathymetry: water column imaging with multibeam echo sounder systems, Hydrogr. Nachr., 31, 6–10, https://oceanrep.geomar.de/id/eprint/23936/1/HN097(1).pdf (last access: 18 September 2024), 2014.

Scott, D. W.: On optimal and data-based histograms, Biometrika, 66, 605–610, https://doi.org/10.1093/biomet/66.3.605, 1979.

Šiljeg, A., Cavrić, B., Marić, I., and Barada, M.: GIS modelling of bathymetric data in the construction of port terminals – an example of Vlaška channel in the port of Ploče, croatia, Int. J. Eng. Model., 32, 17–37, https://doi.org/10.31534/engmod.2019.1.ri.01m, 2019.

Smith, W. H. and Sandwell, D. T.: Bathymetric prediction from dense satellite altimetry and sparse shipboard bathymetry, J. Geophys. Res.-Sol. Ea., 99, 21803–21824, https://doi.org/10.1029/94JB00988, 1994.

Su, D., Yang, F., Ma, Y., Zhang, K., Huang, J., and Wang, M.: Classification of coral reefs in the south China sea by combining airborne LiDAR bathymetry bottom waveforms and bathymetric features, IEEE T. Geosci. Remote, 57, 815–828, https://doi.org/10.1109/TGRS.2018.2860931, 2018.

Thomas, N., Pertiwi, A. P., Traganos, D., Lagomasino, D., Poursanidis, D., Moreno, S., and Fatoyinbo, L.: Space-borne cloud-native satellite-derived bathymetry (SDB) models using ICESat-2 and sentinel-2, Geophys. Res. Lett., 48, e2020GL092170, https://doi.org/10.1029/2020GL092170, 2021.

Tinto, K. J., Padman, L., Siddoway, C. S., Springer, S. R., Fricker, H. A., Das, I., Caratori Tontini, F., Porter, D. F., Frearson, N. P., Howard, S. L., Siegfried, M. R., Mosbeux, C., Becker, M. K., Bertinato, C., Boghosian, A., Brady, N., Burton, B. L., Chu, W., Cordero, S. I., Dhakal, T., Dong, L., Gustafson, C. D., Keeshin, S., Locke, C., Lockett, A., O'Brien, G., Spergel, J. J., Starke, S. E., Tankersley, M., Wearing, M. G., and Bell, R. E.: Ross ice shelf response to climate driven by the tectonic imprint on seafloor bathymetry, Nat. Geosci., 12, 441–449, https://doi.org/10.1038/s41561-019-0370-2, 2019.

Tozer, B., Sandwell, D. T., Smith, W. H., Olson, C., Beale, J., and Wessel, P.: Global bathymetry and topography at 15 arc sec: SRTM15+, Earth Space Sci., 6, 1847–1864, https://doi.org/10.1029/2019EA000658, 2019.

Tysiac, P.: Bringing bathymetry LiDAR to coastal zone assessment: a case study in the southern baltic, Remote Sens., 12, 3740, https://doi.org/10.3390/rs12223740, 2020.

Wang, A., Du, Y., Peng, S., Liu, K., and Huang, R. X.: Deep water characteristics and circulation in the south China sea, Deep-Sea Res. Pt. I, 134, 55–63, https://doi.org/10.1016/j.dsr.2018.02.003, 2018a.

Wang, J., Yi, S., Li, M., Wang, L., and Song, C.: Effects of sea level rise, land subsidence, bathymetric change and typhoon tracks on storm flooding in the coastal areas of shanghai, Sci. Total Environ., 621, 228–234, https://doi.org/10.1016/j.scitotenv.2017.11.224, 2018b.

Warren, M. A., Simis, S. G., Martinez-Vicente, V., Poser, K., Bresciani, M., Alikas, K., Spyrakos, E., Giardino, C., and Ansper, A.: Assessment of atmospheric correction algorithms for the sentinel-2A MultiSpectral imager over coastal and inland waters, Remote Sens. Environ., 225, 267–289, https://doi.org/10.1016/j.rse.2019.03.018, 2019.

Weatherall, P., Marks, K. M., Jakobsson, M., Schmitt, T., Tani, S., Arndt, J. E., Rovere, M., Chayes, D., Ferrini, V., and Wigley, R.: A new digital bathymetric model of the world's oceans, Earth Space Sci., 2, 331–345, https://doi.org/10.1002/2015EA000107, 2015.

Wölfl, A.-C., Snaith, H., Amirebrahimi, S., Devey, C. W., Dorschel, B., Ferrini, V., Huvenne, V. A., Jakobsson, M., Jencks, J., and Johnston, G.: Seafloor mapping–the challenge of a truly global ocean bathymetry, Front. Mar. Sci., 6, 283, https://doi.org/10.3389/fmars.2019.00283, 2019.

Wu, Y., Li, Y., Jia, D., Andersen, O. B., Abulaitijiang, A., Luo, Z., and He, X.: Seamless seafloor topography determination from shallow to deep waters over island areas using airborne gravimetry, IEEE T. Geosci. Remote, 61, 1–19, https://doi.org/10.1109/TGRS.2023.3336747, 2023.

Wu, Y., Shi, H., Jia, D., Andersen, O. B., He, X., Luo, Z., Li, Y., Chen, S., Si, X., Diao, S., Shi, Y., and Chen, Y.: HHU24SWDSCS: a shallow-water depth model over island areas in south China sea retrieved from satellite-derived bathymetry, Zenodo [data set], https://doi.org/10.5281/zenodo.13852568, 28 September 2024a.

Wu, Y., Jia, D., Li, Y., He, X., Baltazar Andersen, O., Luo, Z., and Si, X.: Refinement of marine gravity anomaly over shallow waters by using satellite-derived bathymetry, IEEE T. Geosci. Remote, 62, 1–17, https://doi.org/10.1109/TGRS.2024.3403421, 2024b.

Wu, Y., Andersen, O. B., Abulaitijiang, A., Shi, H., He, X., Jia, D., Luo, Z., and Wang, H.: Seafloor topography modeling by fusing ICESat-2 lidar, echo sounding, and airborne and altimetric gravity data from spherical radial basis functions, IEEE T. Geosci. Remote, 63, 1–17, https://doi.org/10.1109/TGRS.2024.3523893, 2025.

Yang, F., Su, D., Ma, Y., Feng, C., Yang, A., and Wang, M.: Refraction correction of airborne LiDAR bathymetry based on sea surface profile and ray tracing, IEEE T. Geosci. Remote, 55, 6141–6149, https://doi.org/10.1109/TGRS.2017.2721442, 2017a.

Yang, F., Qi, C., Su, D., Ding, S., He, Y., and Ma, Y.: An airborne LiDAR bathymetric waveform decomposition method in very shallow water: a case study around yuanzhi island in the south China sea, Int. J. Appl. Earth Obs., 109, 102788, https://doi.org/10.1016/j.jag.2022.102788, 2022.

Yang, X., Zhao, S., Qin, X., Zhao, N., and Liang, L.: Mapping of Urban Surface Water Bodies from Sentinel-2 MSI Imagery at 10 m Resolution via NDWI-Based Image Sharpening, Remote Sensing, 9, 596, https://doi.org/10.3390/rs9060596, 2017b.

Yen, P. P., Sydeman, W. J., and Hyrenbach, K. D.: Marine bird and cetacean associations with bathymetric habitats and shallow-water topographies: implications for trophic transfer and conservation, J. Marine Syst., 50, 79–99, https://doi.org/10.1016/j.jmarsys.2003.09.015, 2004.

Zhu, S., Li, X., Zhang, H., Sha, Z., and Sun, Z.: Types, characteristics, distribution, and genesis of pockmarks in the south China sea: insights from high-resolution multibeam bathymetric and multichannel seismic data, Int. Geol. Rev., 63, 1682–1702, https://doi.org/10.1080/00206814.2020.1848645, 2021.